

Lawrence Berkeley National Laboratory

LBL Publications

Title

Mineralogy and density of Archean volcanic crust in the mantle transition zone

Permalink

<https://escholarship.org/uc/item/9wg0p6jj>

Authors

Ko, Byeongkwan
Prakapenka, Vitali
Kunz, Martin
et al.

Publication Date

2020-08-01

DOI

10.1016/j.pepi.2020.106490

Peer reviewed

Mineralogy and Density of Archean Volcanic Crust in the Mantle Transition Zone

Byeongkwan Ko^{a,*}, Vitali Prakapenka^b, Martin Kunz^c, Clemens Prescher^{b,d}, Kurt Leinenweber^a, Sang-Heon Shim^{a,*}

^a*School of Earth and Space Exploration, Arizona State University, Tempe, Arizona 85287, United States*

^b*Center for Advanced Radiation Sources, University of Chicago, Chicago, Illinois 60439, United States*

^c*Advanced Light Source, Lawrence Berkeley National Laboratory, Berkeley, California 94720, United States*

^d*Now at Photon Sciences, Deutsches Elektronen-Synchrotron (DESY), Hamburg 22607, Germany*

Abstract

The composition of Archean volcanic crust can be characterized by a higher Mg/Si ratio than modern mid-ocean ridge basalt (MORB), because of the higher degree melting from the warmer mantle in the Archean. Although modern MORB may become less dense than the surrounding mantle beneath the mantle transition zone (MTZ), the Mg-rich composition of Archean volcanic crust may result in the different density, and therefore different sinking behavior near the MTZ. In order to understand the compositional effect of Archean volcanic crust on the sinking behaviors and the scale of mantle mixing in the Archean, we investigated the mineralogy and density of Archean volcanic crust near the MTZ (470–910 km-depth). We conducted experiments at 19–34 GPa and 1,400–2,400 K using the laser-heated diamond anvil cell (LHDAC) combined with in-situ X-ray diffraction (XRD). The in-situ XRD and the chemical analysis revealed that Archean volcanic crust forms garnet and ringwoodite (84 and 16 vol%), which gradually transforms to Brg and CaPv (82 and 18 vol%) at 23–25 GPa and 1,800 K. Our in-situ XRD experiments allowed us to measure the volumes of stable phases and to estimate their densities at high pressure and temperature. The results suggest that Archean volcanic crust maintains greater density than the pyrolitic mantle in the Archean regardless of temperature at 20–34 GPa (570–850 km-depth), promoting further sinking

*Corresponding authors

Email addresses: byeongkw@asu.edu (Byeongkwan Ko), SHDShim@gmail.com (Sang-Heon Shim)

into the deeper mantle in the Archean. We also considered the density of the subducting slab in the Archean. The density model showed that the subducting slab is still denser or at least equally dense as the surrounding pyrolitic mantle in the Archean.

Keywords: Archean volcanic crust, Density, Mineralogy, Mantle transition zone, In-situ X-ray diffraction, High P - T experiments

1 **1. Introduction**

2 Surface materials have been transported into the deep mantle and played vital roles
3 in mantle geochemistry and dynamics for billions of years in the Earth's history (e.g.,
4 Van Hunen and Moyen, 2012; Laurent et al., 2014; Tang et al., 2016; Condie, 2018).
5 Seismic tomography images have shown stagnation of the slabs beneath the mantle
6 transition zone (MTZ) in the Western Pacific (e.g., van der Hilst and Seno, 1993; Fukao
7 et al., 2009; Li and McNamara, 2013; King et al., 2015). Indeed, sinking of the slabs
8 into the deep mantle can be challenged beneath the MTZ at 670–760 km-depth (Chris-
9 tensen, 1997; Ogawa, 2003; Davies, 2008; Klein et al., 2017) where the density of the
10 surrounding mantle increases dramatically because of the post-spinel transition (Hi-
11 rose, 2002; Ye et al., 2014; Ishii et al., 2018).

12 While the density of the modern subducting slab has been well documented at high
13 pressures and high temperatures (Hirose et al., 1999; Irifune and Ringwood, 1993;
14 Ringwood and Irifune, 1988), the density of the early Earth's materials is not the case.
15 In the Archean, the mantle potential temperature was likely much greater than present
16 day by approximately 200 K (Korenaga, 2008; Herzberg et al., 2010). The high tem-
17 perature results in the more extensive partial melting in the Archean, resulting in two
18 important differences for Archean volcanic crust. First, Archean volcanic crust forms
19 with a much greater MgO content than present-day mid ocean ridge basalt (MORB;
20 Table 1) (Herzberg et al., 2007, 2010). The different composition of Archean volcanic
21 crust would lead to different mineralogy and density at high pressure-temperature (P -
22 T) conditions in the mantle. Second, the thickness of the crust should be much greater
23 in the Archean (up to 45 km-thick) than in the modern day (7 km-thick; Herzberg et al.,
24 2010; Herzberg and Rudnick, 2012). With the large thickness, Archean volcanic crust

25 takes a large portion of the subducting slab in the Archean, and therefore plays a more
26 important role in the sinking behavior of the subducting slab.

27 Archean volcanic crust could have been transported into the mantle through a range
28 of different processes: delamination (e.g., Bédard, 2006; Johnson et al., 2014), and
29 subduction (e.g., Laurent et al., 2014; Tang et al., 2016; Condie, 2018). For the case
30 of subduction, timing for the onset of modern-style plate tectonics is still under debate.
31 Multiple lines of geochemical evidence suggest that modern-style global subduction
32 would have occurred since 2.0–3.5 Ga (Laurent et al., 2014; Tang et al., 2016; Condie,
33 2018). Subduction style in the Archean could have been episodic (Van Hunen and
34 Moyen, 2012). Geodynamic modeling has shown that the hotter mantle in the Archean
35 results in weak subducting slabs, leading to frequent break-off of the slabs (Van Hunen
36 and Moyen, 2012).

37 If Archean volcanic crust remains as a heterogeneity in the present-day mantle
38 owing to the slow chemical diffusion at high pressure (Holzapfel et al., 2005; Stixrude
39 and Lithgow-Bertelloni, 2012; Xu et al., 2011; Ito and Toriumi, 2010), the behavior
40 of such heterogeneity is also important for understanding the origin of the seismic
41 heterogeneities found in the mantle (e.g. Fukao et al., 2009; Fukao and Obayashi, 2013;
42 Wu et al., 2019).

43 It is also of interest if Archean volcanic crust would have contributed to the rise of
44 atmospheric O₂ at approximately 2.4 Ga (the Great Oxidation Event or GOE) (Kasting,
45 2013). The MgO-rich composition might have resulted in the more extensive H₂
46 production through serpentinization than in the modern day (Kasting, 2013). The com-
47 positional change in the volcanic crust during the mantle cooling might have reduced
48 such H₂ production, leading to the accumulation of O₂ in the atmosphere. In addi-
49 tion, the recent measurements of the V partitioning in ancient volcanic rocks suggested
50 that the reducing Archean upper mantle might have undergone the secular oxidation
51 between 3.5 and 1.9 Ga (Nicklas et al., 2019). Possible mechanisms for the oxidation
52 processes include not only the compositional change of the volcanic crust recycled into
53 the mantle, but also homogenization of the redox state of the mantle by effective man-
54 tle mixing (Nicklas et al., 2019; Aulbach and Stagno, 2016). The style of the mantle
55 convection in the Archean could have been also affected by the changes in the tectonic

56 mode. It is possible that the subducting slabs might have facilitated the whole man-
57 tle mixing with the primordial oxidizing materials stored in the lower mantle (Nicklas
58 et al., 2019; Aulbach and Stagno, 2016; Andraut et al., 2018a).

59 The composition of the Archean materials sunken to the mantle has been modeled
60 with komatiitic compositions (e.g. Nishihara and Takahashi, 2001; Klein et al., 2017).
61 Nishihara and Takahashi (2001) conducted multi-anvil experiments and calculated the
62 density of komatiite with thermodynamic parameters and the calculated zero-pressure
63 densities of the synthesized phases. They showed that the density of komatiite is greater
64 than the PREM density in the MTZ up to 23 GPa. The density of the surrounding man-
65 tle in the Archean is likely lower than the PREM density (i.e., present-day mantle den-
66 sity) because of the higher temperature. Therefore, the density contrast between their
67 komatiite and the Archean mantle may be even greater. However, their komatiite com-
68 position may not be representative Archean volcanic crust formed by partial melting
69 of the mantle, because of the higher MgO content (32 wt%) and the lower Al₂O₃ con-
70 tent (4 wt%) compared to non-arc basaltic compositions in the Archean (23 and 9 wt%,
71 respectively; Herzberg et al., 2010; Johnson et al., 2014, ; Table 1). Furthermore, the
72 density was not directly measured at high P - T .

73 Klein et al. (2017) has recently studied the density of komatiitic composition at
74 depths of the MTZ and the topmost lower mantle using a thermodynamic modelling
75 program, *Perple_X* (Connolly, 2009). They used a less MgO-rich komatiitic composi-
76 tion (26 wt% of MgO) for Archean volcanic crust (Herzberg et al., 2010). The model
77 predicted that komatiite is denser than the pyrolitic Archean mantle in the MTZ and
78 the topmost lower mantle, supporting the likelihood of the sinking of the materials into
79 the lower mantle.

80 However, unlike other compositions, such as modern MORB and pyrolite which
81 have been cross-examined by theoretical calculations (Xu et al., 2008; Stixrude and
82 Lithgow-Bertelloni, 2012) and in-situ experiments (Ricolleau et al., 2010; Hirose et al.,
83 2005), the density of the Archean volcanic crustal composition has not been directly
84 measured by in-situ experiments. Also, it would be worthwhile to explore differences in
85 mineralogy and density between komatiite and modeled compositions (Johnson et al.,
86 2014) for Archean volcanic crust. More importantly, no study has explored the com-

87 bined density of the crust and harzburgitic layer for the Archean subducting slabs. The
88 lack of such consideration limits our understanding of the sinking behaviors of the
89 Archean subducting slabs.

90 As mentioned above, Archean volcanic crust is different from modern MORB in
91 two aspects: 1) much more MgO-rich composition and 2) greater thickness (Korenaga,
92 2008; Herzberg et al., 2010). Because of these differences, Archean volcanic crust
93 would have played a different role in the sinking behaviors of the Archean subduct-
94 ing slabs than modern MORB does. It would be particularly important to address a
95 question of how sinking behaviors of subducting slabs may have evolved over time as
96 Earth's mantle cools.

97 Here, we report experimental results on the composition for Archean volcanic
98 crust at pressures of 19–34 GPa and temperatures of 1,400–2,400 K. Our in-situ X-ray
99 diffraction provides direct measurements of the unit-cell volumes of the stable phases,
100 allowing us to estimate the densities at high P – T . We also explored the effects of
101 harzburgite layer using *Perple_X*, for the case where Archean volcanic crust is trans-
102 ported to the MTZ through subduction style.

103 [Table 1]

104 **2. Experimental Methods**

105 *2.1. Starting material*

106 We synthesized a homogeneous glass using the laser-levitation method (Tangeman
107 et al., 2001) under a reducing condition (1:1 ratio of the gas mixture CO:CO₂). The
108 chemical composition of the starting material was obtained from the partial melting
109 model by Johnson et al. (2014) (Table 1). The model assumes that the MgO and FeO
110 contents of the crustal composition linearly increase with an increase in the mantle
111 potential temperature (T_P) based on the reported chemical compositions of a range of
112 non-arc volcanic crustal compositions from 3.5 Ga to the present day (Johnson et al.,
113 2014; Herzberg et al., 2007, 2010; Palin and White, 2016). From this model, we chose
114 the composition for Archean volcanic crust (2.5–3.0 Ga; hereafter B30) that might have

115 formed at a T_P of $\sim 1,900$ K. We confirmed successful synthesis of the starting mate-
116 rial in an electron probe micro analyzer (JEOL JXA-8530F EPMA) combined with
117 wavelength-dispersive X-ray spectrometer (WDS) at Arizona State University (ASU)
118 (Table 1). We did not measure the $\text{Fe}^{3+}/\Sigma\text{Fe}$ in the starting material.

119 2.2. *Laser-heated diamond-anvil cell experiments*

120 The powdered glass was mixed with ~ 10 wt% of Au powder (grain size of $1\text{--}3\ \mu\text{m}$),
121 which served as a pressure standard and a laser absorber in the laser-heated diamond-
122 anvil cell (LHDAC) experiments. The mixture was compressed to thin foils with a
123 size of $100\text{--}200\ \mu\text{m}$ and a thickness of $\sim 10\ \mu\text{m}$. Then, the foil was loaded into a hole
124 in a pre-indented rhenium gasket with a micro-manipulator (Microsupport Axis Pro
125 SS) at ASU. We placed four spacers ($<10\ \mu\text{m}$ sized pure sample particle) between the
126 sample foil and each side of the diamond culets for the gas or liquid medium loading.
127 We loaded Ne and Ar in the COMPRES-GSECARS high-pressure gas loading system
128 (Rivers et al., 2008) or the cryogenic liquid loading system at ASU. For the solid
129 media (NaCl and KCl), powder was dried at 120°C for 4 hours before loading. The
130 solid media were prepared as foils and placed below and above the sample foil in the
131 sample chamber. We compressed the samples in the symmetric-type diamond-anvil
132 cell. The samples were compressed with diamond anvils ($400\ \mu\text{m}$ -sized culet).

133 We have conducted LHDAC experiments combined with in-situ X-ray diffraction
134 (XRD) at sector 13-IDD of the GeoSoilEnviroConsortium (GSECARS) in the Ad-
135 vanced Photon Source (APS) (Prakapenka et al., 2008) (Tables S1 and S2). The pres-
136 sure and temperature ranges of the experiments were $19\text{--}34$ GPa and $1,400\text{--}2,400$ K,
137 respectively. For run #4430 only, we synthesized the sample in LHDAC at ASU and
138 then measured diffraction patterns at high pressure and room temperature in DAC at
139 sector 12.2.2 in the Advanced Light Source (ALS) (Table S1). The wavelengths of the
140 monochromatic X-ray beams were 0.3344 , 0.4133 , and $0.4959\ \text{\AA}$ for GSECARS and
141 $0.4971\ \text{\AA}$ for ALS. For in-situ experiments, we focused the laser beams on both sides
142 of the sample and aligned the laser beams coaxially with the X-ray beam by visually
143 observing X-ray fluorescence, in order to measure XRD patterns at the center of the
144 laser heating spot. Typical beam diameters for the X-ray focus and the laser hotspot on

145 the sample in LHDAC were ~ 5 and $20\ \mu\text{m}$, respectively. We fit the thermal radiation
146 spectra measured from both sides of the sample to Planck gray-body equation for the
147 estimation of temperature. We attached a gas membrane to the LHDAC for fine control
148 of pressure during in-situ laser heating (Letoullec et al., 1988), except for run #218
149 where the pressure was increased manually to the target pressure.

150 We measured diffraction images using a MarCCD or a Dectris Pilatus detector at
151 GSECARS. For run #4430, diffraction images were collected with a Mar345 detec-
152 tor at ALS. The diffraction images were integrated to 1D diffraction patterns with
153 the calibration parameters obtained from the LaB_6 standard in the DIOPTAS software
154 (Prescher and Prakapenka, 2015). Diffraction images were collected for 5–10 seconds
155 to ensure enough quality for data analysis. For run #4430 at ALS, we exposed the de-
156 tector for 120–300 seconds. The collected diffraction patterns were analyzed and fitted
157 with a pseudo-Voigt profile function to obtain the peak positions in the PeakPo soft-
158 ware (Shim, 2017a). We obtained unit-cell parameters using the PeakPo and UnitCell
159 softwares (Holland and Redfern, 1997). We determined pressures with the equation
160 of state (EOS) of Au (Dorogokupets and Dewaele, 2007) using the Pytheos software
161 (Shim, 2017b). The pressures at high temperatures were further corrected according to
162 Ye et al. (2017). The unit-cell volume of Au was calculated from the 2–5 diffraction
163 lines for majority of the data points.

164 We heated multiple spots in each sample and avoided areas that are close to the
165 Re gasket. For each heating spot, an area with a diameter of $20\ \mu\text{m}$ was heated for up
166 to 11 minutes (Table S1). The locations of heating spots were chosen with an enough
167 distance up to $30\ \mu\text{m}$ from the previously heated areas in order to start a new heating
168 cycle with unheated fresh areas.

169 In-situ XRD patterns showed that our glass sample transformed into crystalline
170 phases within 5–60 seconds depending on temperature. Once formed, the XRD peak
171 intensities of crystalline phases gradually grow over time without significant changes
172 in the further heating. For most runs, the laser power was first increased at a previously
173 heated spot until a target temperature is reached, and then instantly translated to an
174 unheated amorphous area such that the new area can reach target temperature directly.
175 This heating method helps preventing kinetic effects because the amorphous starting

176 material does not experience low temperatures during gradual increase in laser power
177 in typical laser heating experiments.

178 [Fig. 1]

179 2.3. Chemical analysis

180 We recovered the synthesized samples from runs #218 and #4430 in a micro-
181 manipulator. The samples were processed for the STEM measurements in a focused ion
182 beam (FIB; FEI Nova 200 and FEI Helios) at ASU and University of Arizona (UofA),
183 respectively. We extracted the center part of the heated area and mounted it on a Cu
184 or Mo grid. The composition of the sample was analyzed in the aberration-corrected
185 scanning transmission electron microscope (STEM): JEOL ARM200F at ASU and Hi-
186 tachi HF-5000 at UofA combined with energy-dispersive X-ray spectroscopy (EDS).
187 A 120 and 200 keV of acceleration voltages were used at ASU and UofA, respectively.
188 We measured standard spectra from the starting glass material for the data analysis. We
189 performed a 2D chemical mapping for run #4430 and then estimated volume fractions
190 of phases from the area fraction (Fig. 1). We also performed a point analysis with ex-
191 posure time of 20–40 seconds depending on the beam sensitivity at a target grain. The
192 collected EDS spectra were fitted using a python code LMFIT (Newville et al., 2016).

193 [Fig. 2]

194 3. Experimental results

195 We have found three distinct P – T fields with different mineralogy in our exper-
196 iments (Fig. 2): garnet-dominant (Gt-dominant), garnet-bridgmanite-transition (Gt-
197 Brg-transition), and bridgmanite-dominant (Brg-dominant) P – T fields (Fig. 3).

198 [Fig. 3]

199 3.1. Garnet-dominant P – T field

200 Between 19 and 25 GPa, we observed Gt and ringwoodite (Rw) as stable phases
201 (Fig. 2a). The diffraction intensities indicates that Gt represents the major phase of the
202 mineralogy (Fig. 3). We employed the Rietveld refinement using GSAS-II (Toby and
203 Von Dreele, 2013) and obtained 86.5 and 14.5 vol% for Gt and Rw, respectively, which

204 is supported by our STEM observations (Table 2). Fig. 1 shows a high-angle annular
205 dark-field (HDADF) image of the sample from run #4430 which was synthesized at
206 19.5 GPa (pressure measured at 300 K) and 1,900 K in LHDAC. The chemical maps
207 of the image shows that Gt exists as matrix that surrounds the Rw grains. From the
208 STEM-EDS images, we obtained 85.3 and 14.7 vol% for the area proportions of Gt
209 and Rw, respectively, consistent with our mass-balance calculation, which yielded 82.7
210 and 17.3 vol% of Gt and Rw, respectively (Table 2).

211 $\text{Fe}^{3+}/\Sigma\text{Fe}$ was not measured for the recovered sample in this study. Because the
212 starting glass was synthesized in the reducing condition, we expect the dominant va-
213 lence state of Fe is Fe^{2+} . If $\text{Fe}^{3+}/\Sigma\text{Fe}$ was large in the synthesized samples, the phase
214 proportion of Gt would be even larger because Gt can accommodate the large amount
215 of Fe^{3+} in the crystal structure, unlike Rw (McCammon and Ross, 2003).

216 The modern MORB mineralogy features Gt as the most abundant component (60–
217 90 vol%) (Irifune and Ringwood, 1993; Litasov and Ohtani, 2005) as does B30 min-
218 eralogy (86 vol%; Table 2). However, stable minor phases are significantly different
219 between these two compositions. The $(\text{Mg}+\text{Fe}+\text{Ca})/\text{Si}$ ratio of B30 is higher than 1
220 (~ 1.15) and therefore excess MgO and FeO can form Rw in addition to Gt as ob-
221 served in our experiments. On the other hand, in the modern MORB composition the
222 $(\text{Mg}+\text{Fe}+\text{Ca})/\text{Si}$ ratio is low enough (0.63) to form stishovite (Stv) from excess silica
223 content (Gale et al., 2013). In addition, the greater Al content (15.5 wt%) in modern
224 MORB adds Al-rich phase to the mineralogy, whereas nearly all Al is incorporated in
225 Gt in B30 (8.6 wt%). The mineralogy of the modern MORB composition consists of
226 Gt, Stv, CaPv, and Al-phase, in an order of their abundances, at 15–26 GPa and 1,473–
227 2,573 K (Irifune et al., 1986; Irifune and Ringwood, 1993; Hirose and Fei, 2002).

228 At a similar pressure range, pyrolite has Rw (or Wd), Gt, CaPv, and akimotoite
229 (Aki) in an order of abundance (Hirose, 2002; Ye et al., 2014; Ishii et al., 2018). Py-
230 rolite has a much higher $(\text{Mg}+\text{Fe}+\text{Ca})/\text{Si}$ ratio (1.49) than modern MORB and B30
231 (Table 1), making Rw (or Wd) the most abundant phase in the mineralogy. As shown
232 in Table 2, Gt represents 84 vol% in B30, whereas Rw represents 60 vol% in pyrolite
233 (Irifune et al., 2010; Ishii et al., 2018).

234 The chemical composition of Gt is significantly different among B30, modern

235 MORB, and pyrolite (Table S2). Compared to B30, Gt in modern MORB has twice
236 more Al_2O_3 (8.6 and 20.6 wt%, respectively) and half as many MgO (20.9 and 12.3 wt%,
237 respectively) as B30 has (Hirose and Fei, 2002). Gt in pyrolite has nearly half as much
238 FeO (5.0 and 11.8 wt%, respectively) and CaO (4.6 and 9.0 wt%) as B30 does, but
239 slightly more MgO than in B30 (Hirose, 2002). These compositional differences are
240 important to consider for the density and velocity profiles.

241 [Table 2]

242 3.2. Garnet-bridgmanite-transition P - T field

243 At intermediate pressures in our experiments, we observed the Gt-Brg-transition
244 P - T field in B30 (Fig. 3). Above 23 GPa, Rw disappears and Brg appears, suggesting
245 the occurrence of the post-spinel transition where Rw decomposes into Brg and fer-
246 ropericlasite (Fp). While the diffraction peak intensities show that Gt is still the major
247 phase in the Gt+Brg mineralogy (Fig. 2), we could not resolve Fp in XRD patterns
248 because of the peak overlap with Ar, Gt, or Brg peaks. Furthermore, the peak inten-
249 sities of Fp is expected to be small because of the possible reduction process in the
250 amount of Fp. Brg is known to have high capacity for Fe^{3+} through the charge dispro-
251 portionation reaction: 3FeO to $2\text{Fe}_2\text{O}_3$ and Fe metal (Frost et al., 2004). If a significant
252 fraction of Fe is Fe^{3+} , the more Brg can form by the coupled-substitution of $\text{Mg}^{2+} +$
253 Si^{4+} with $\text{Fe}^{3+} + \text{Al}^{3+}$, and therefore reduce the available FeO for Fp in the system
254 (e.g., McCammon, 1997; Andraut et al., 2001). We estimated $\text{Fe}^{3+}/\sum\text{Fe}$ in Brg based
255 on the measured compositions by assuming the charge-balanced substitutions of Fe^{3+}
256 and Al^{3+} . The estimation yields approximately 0.57 for $\text{Fe}^{3+}/\sum\text{Fe}$, which is consistent
257 with previous reports (e.g. Shim et al., 2017). However, we note that this estimation
258 method for $\text{Fe}^{3+}/\sum\text{Fe}$ is very sensitive to the Si# in the stoichiometric composition
259 of Brg, and therefore the large uncertainties are involved given the error range of the
260 EDS quantitative analysis ($\sim 10\%$). We did not observe Fe metal in either STEM ob-
261 servations or XRD patterns, perhaps because of the expected small amount of Fe metal
262 (Section 3.3). Although the limited number of data points increases the uncertainties,
263 the P - T slope of Brg-in boundary was roughly estimated to be -0.8 ± 0.3 MPa/K, in
264 a good agreement with the Clapeyron slope of the post-spinel transition from previous

265 studies (e.g. Katsura et al., 2003; Litasov et al., 2005; Ishii et al., 2011, 2018).

266 At higher pressures above 1,600 K, CaPv was observed alongside Gt and Brg. The
267 diffraction peak intensities of Brg are in general stronger in the Gt+Brg+CaPv mineral-
268 ogy than in the Gt+Brg mineralogy. These observations suggest the post-Gt transition
269 where Gt decomposes into CaPv and Brg. We observed the two phase boundaries
270 for the post-Gt transition with 1.7 GPa of the pressure interval: the CaPv-in bound-
271 ary and Gt-out boundary. The P - T slopes of these boundaries were determined to be
272 3.5 ± 0.5 MPa/K, which is in the middle of the range of the Clapeyron slopes of the
273 post-Gt transition in previous studies (Hirose et al., 1999; Kubo and Akaogi, 2000;
274 Oguri et al., 2000; Hirose, 2002; Litasov et al., 2004; Ishii et al., 2018). Note that the
275 uncertainties of the P - T slopes may be large due to the limited number of data points
276 across the boundaries. The gradual post-Gt transition has been reported by earlier ex-
277 periments of Al-bearing Gt (Irifune et al., 1996) up to 2.1 GPa of an interval at 1,773 K
278 for 3–11 mol% of Al_2O_3 . Gt in B30 contains 4.8 mol% of Al_2O_3 which is estimated
279 to yield 1.1 GPa interval for the post-Gt transition according to Irifune et al. (1996).
280 However, Gt in B30 also contains a significant amount of FeO (11.8 wt%; Table 1), the
281 effect of which on the pressure interval of the post-Gt transition is not well known.

282 The opposite signs of P - T slopes of the post-spinel and post-Gt transitions (-0.8 ± 0.3
283 and 3.5 ± 0.5 MPa/K, respectively) results in the wider stability of the Gt-Brg-transition
284 P - T field with an increase in temperature above 1,600 K. Below 1,600 K, we do not
285 have sufficient number of data points due to the large kinetic effects at lower tempera-
286 tures. One run at 22.6 GPa and 1,570 K (the green diamond in Fig. 3) shows the signs
287 of Brg 112, 200, and 220 lines and strong CaPv 110 line in the XRD pattern, alongside
288 the strong Gt and Rw lines. These observations are in line with CaPv-in boundary ob-
289 served from the higher temperatures, suggesting that the post-Gt transition may occur
290 at shallower depths than the post-spinel transition at lower temperatures.

291 The most noticeable difference in mineralogy between modern MORB and B30 at
292 the intermediate pressure range is the depths of Brg-in and Gt-out boundaries (Fig. 3b).
293 For example, at 1,700 K Brg-in boundary appears as the post-spinel transition at a lower
294 pressure of 23 GPa in B30 than the post-Gt transition at 25.8 GPa in modern MORB
295 (Hirose et al., 1999). The Si-rich composition of modern MORB does not form Rw in

296 the mineralogy, resulting in the absence of the post-spinel transition, which can occur
297 at the shallower depth than the post-Gt transition. Then, Gt completely transformed
298 to Brg at 24.8 GPa in B30, whereas Gt persists until 26.8 GPa in modern MORB (60–
299 70 vol%) (Hirose et al., 1999; Irifune and Ringwood, 1993; Litasov and Ohtani, 2005).
300 The difference in the depth and the P – T slope of Gt-out boundary between B30 and
301 modern MORB is likely caused by the compositional difference in Gt (Table S2).

302 Pyrolite has similar mineralogy as B30 in the Gt-Brg-transition P – T field. In py-
303 rolitic composition, Gt and Brg coexist as major components (Hirose, 2002; Ishii et al.,
304 2018) at 22–26 GPa. Also, pyrolite exhibits the negative slope for Brg-in boundary be-
305 cause of the post-spinel transition. Brg-in boundary appears at a nearly same pressure
306 in B30 and pyrolite: 22.8 and 22.6 GPa at 1,900 K, respectively (Ishii et al., 2018). On
307 the other hand, the Gt-out boundary appears at a higher pressure in B30 than in pyrolite
308 by 1.1 GPa: 25.5 and 24.4 GPa at 1,900 K, respectively (Ishii et al., 2018).

309 3.3. Bridgmanite-dominant P – T field

310 At pressures above 25 GPa, the mineralogy of B30 becomes Brg and CaPv (Fig. 3).
311 The diffraction intensities show that Brg is the major phase in the Brg+CaPv system
312 (Fig. 2). The (Mg+Fe+Ca)/Si ratio of B30 is higher than 1 (1.15), the excess MgO
313 and FeO can stabilize Fp together with Brg and CaPv, if the majority of Fe is Fe²⁺.
314 However, we could not identify Fp peaks in the diffraction patterns because of the ex-
315 pected peak overlap with the Brg peaks. Fp was not observed in TEM analysis either.
316 The amount of Fp might have been too small to be detected because the disproportion-
317 ation reaction of Brg (Section 3.2; Frost et al., 2004) can reduce the available number
318 of Fe²⁺ for Fp. Although the heating duration was adequately controlled in our ex-
319 periments within 8 mins (Table S1), we do not rule out the possibility that the Soret
320 diffusion caused the Fe loss in the heating center (Sinmyo and Hirose, 2010). Some
321 amount of FeO or Fe metal might have migrated away from the heating center to the
322 low-temperature regions. The calculated phase proportions based on the measured
323 compositions by TEM-EDS (Table 2) yield only 1±1 vol% of Fp. For Brg and CaPv,
324 81.6 and 18.4 vol% were obtained by the mass-balance calculations, consistent well
325 with 82.2 and 17.8 vol% from Rietveld refinements within 1 % of difference (Table 2).

326 As described in Section 3.1, the starting material was synthesized under a reducing
327 condition. Even if $\text{Fe}^{3+}/\Sigma\text{Fe}$ was larger in the synthesis products, the phase proportion
328 of Brg would be still large because Brg is the only phase that can incorporate Fe^{3+} in
329 the mineralogy in the Brg-dominant P - T field.

330 Modern MORB contains much lower content of Brg than B30 at P - T conditions of
331 the lower-mantle. Modern MORB contains 30, 27, 22, and 21 vol% of CaPv, aluminous
332 phase, Stv, and Brg, respectively at 31 GPa (Ricolleau et al., 2010). Pyrolite and B30
333 are much alike in that Brg is abundant (75, 18, and 7 vol% for Brg, Fp, and CaPv,
334 respectively, at above 27 GPa for pyrolite; Irifune et al. (2010); Ishii et al. (2018)), but
335 different in that B30 contains very small or no Fp in the mineralogy.

336 [Fig. 4]

337 4. Density profiles

338 4.1. Density profile of Archean volcanic crust

339 We estimated the density profiles of Archean volcanic crust (B30) along the low
340 and equilibrated temperature profiles in the Archean (hereafter referred to as AL and
341 AE, respectively). The AL temperature was obtained from the temperature model of
342 the subducting slab in Klein et al. (2017). For the AE temperature, we assumed the
343 same temperature as the surrounding mantle in the Archean, which was shifted from
344 the modern mantle geotherm (Brown and Shankland, 1981) by 200 K (Korenaga, 2008;
345 Herzberg et al., 2010). Fig. S2 compares the geotherm models with the adiabatic tem-
346 perature gradients.

347 Our in-situ XRD experiments provided the direct measurements of the unit-cell
348 volumes of the stable phases at high P - T . We considered Gt, Rw, Brg, and CaPv at
349 20–34 GPa. For the Gt+Rw mineralogy, the chemical compositions and phase pro-
350 portions of Gt and Rw were obtained from our STEM-EDS measurements, which were
351 assumed to remain unchanged within the same mineralogy field (Table 2). At pressures
352 above Brg-in boundary and below CaPv-in boundary, we took Fp into account the min-
353 eralogy (Gt+Brg+Fp) and density calculations. The measured Rw composition was
354 used to model the compositions and proportions of Brg and Fp, which form through

355 the post-spinel transition. The unit-cell volumes of Fp were calculated by the equa-
356 tion of state from Speziale et al. (2007). At pressures above CaPv-in boundary (for the
357 Gt+Brg+CaPv mineralogy), the compositions of Brg and CaPv were obtained from our
358 STEM-EDS measurements and assumed to remain unchanged (Table 2). Their propor-
359 tions were obtained by mass-balance calculations based on the gradual transformation
360 of Gt into Brg and CaPv. At pressures above Gt-out boundary (for the Brg+CaPv min-
361 eralogy), the compositions and proportions of Brg and CaPv were assumed to remain
362 unchanged (Table 2). More information on the density profile model can be found in
363 Text S1.

364 We also calculated the density of pyrolite in the Archean for comparisons with the
365 B30 density (See Section 4.3 for the method). Fig. 4 shows that the B30 density is
366 greater than the pyrolite density in the Archean at most depths between 20–34 GPa
367 (570 and 900 km). The pyrolite density shows a sharp increase at 23–23.5 GPa because
368 of the post-spinel transition, followed by the gradual increase, contributed by the post-
369 Gt transition that occurs in the larger pressure interval (22.5–28 GPa) at the elevated
370 mantle temperature in the Archean.

371 The similar patterns of the phase transitions are observed in B30. The B30 density
372 along the AE temperature markedly increases over a pressure interval of 25–26 GPa
373 (Fig. 4), because of the phase transformation of Gt and Rw into Brg (Section 3.2).
374 The post-spinel transition in B30 at 23 GPa may not increase the density as much as
375 in pyrolite because the lower proportions of Rw (16 and 60 vol%, respectively; Irifune
376 et al. (2010); Ishii et al. (2018)) forms the limited amount of Brg. The B30 density
377 becomes slightly lower than the pyrolite density at 24–25 GPa. However, the Gt-out
378 boundary of the post-Gt transition is at shallower depth in B30 than in pyrolite (26
379 and 28 GPa, respectively) because of the narrower transition thickness (1.7 GPa of the
380 pressure interval) in B30. As a result, B30 becomes denser than pyrolite by 0.1 g/cm³
381 above 25 GPa in the AE temperature (Fig. 6a).

382 In the AL temperature, the B30 density is always greater than the pyrolite density
383 at 20–34 GPa (Fig. 4). The B30 density notably increases at 24–25 GPa because of
384 the post-Gt transition with the narrow pressure interval (1.7 GPa). The density along
385 the AL temperature is greater than along the AE temperature, because of the thermal

386 expansion. On the other hand, the B30 density along the colder temperatures was not
387 investigated in this study due to the limited number of data points at low temperatures.
388 However, we speculate that the B30 density along the colder temperatures should be
389 even greater than the densities in the AE and AL temperatures because the depths
390 of phase transition into Brg will be shallower and the volumes of the phases will be
391 smaller with lower temperatures.

392 [Fig. 5]

393 4.2. Comparisons of the B30 density between experiments and *Perple_X*

394 To examine possible differences between experiments and theoretical calculations,
395 we used *Perple_X* (Connolly, 2009) to calculate the densities of B30 for the AL and
396 AE temperatures and compared with our experiments. In *Perple_X*, we used the Mie-
397 Grüneisun formulation from Stixrude and Lithgow-Bertelloni (2005) and the thermo-
398 dynamic data of mineral phases from Stixrude and Lithgow-Bertelloni (2011), which
399 has been widely used for multi-phase assemblages in the Earth's mantle conditions
400 (e.g., Nakagawa et al., 2010; Stixrude and Lithgow-Bertelloni, 2012; Klein et al., 2017).

401 The B30 density appears to be in a good agreement between the experiments and
402 the *Perple_X* model except for 24.5–28 GPa, where the density from the experiments
403 becomes much greater (Fig. 4). The transition thickness of the post-Gt transition is
404 narrower in the experiments than in the *Perple_X* model (1.7 and 5 GPa, respectively).
405 The B30 density above 28 GPa in the experiments is in a good agreement with that in
406 the *Perple_X* model.

407 Brg-in boundary is consistent with each other within 1% (23.6 and 23.4 GPa, re-
408 spectively), whereas the Gt-out boundary is considerably at higher pressure in the *Per-*
409 *ple_X* model than in our experiments (28.1 and 24.8 GPa at 1,700 K, respectively). The
410 discrepancy results in the greater density in the experiments than in the *Perple_X* model
411 at 24.8–28 GPa (Fig. 4). However, the Clapeyron slopes of the post-spinel and post-Gt
412 transitions are in an excellent agreement between the experiments and *Perple_X* cal-
413 culations. The experiments yielded -0.8 ± 0.3 and 3.5 ± 0.5 MPa/K, whereas *Perple_X*
414 predicted -0.81 MPa/K and 3.1 MPa/K for the post-spinel transition and the post-Gt
415 transition, respectively.

416 On the other hand, the predicted mineralogy by Perple_X was somewhat different
417 from the experiments (Fig. 5). While the major phases, such as, Gt and Brg are the
418 same with different proportions between the experiments and the Perple_X model, the
419 minor phases are additionally predicted from the Perple_X model. For example, in the
420 AL temperature, the Perple_X mineralogy model shows Stv up to 3 vol% together with
421 either Rw or Fp at 21–25 GPa, unlike our experiments (Fig. 5). In the AL and AE tem-
422 peratures, the Perple_X mineralogy model predicted 10 vol% of calcium-ferrite phase
423 above 26 GPa, which was not observed from the experiments. In addition, the Perple_X
424 mineralogy model shows Fp above 24 GPa up to 5 vol%, which was not observed from
425 the experiments either. This is likely caused by the lack of consideration of Fe^{3+} in
426 Brg from the Perple_X model, which ignores a reduced amount of Fe^{2+} through the
427 charge disproportionation reaction (Section 3.2; Frost et al., 2004). Our stoichiometric
428 estimation of Brg from the experiments yields $\text{Fe}^{3+}/\Sigma\text{Fe}=57\%$ (Section 3.2), which is
429 in a good agreement with the reported values (Frost et al., 2004; Shim et al., 2017).

430 [Fig. 6]

431 4.3. Density difference between the volcanic crust and pyrolite

432 Fig. 6a,b shows the density difference of B30 and modern MORB with respect to
433 pyrolite (the surrounding mantle) in the Archean and modern day, respectively. The
434 B30 density is directly from our experiments (Section 4.1). The densities of mod-
435 ern MORB and pyrolite were calculated from Perple_X (Section 4.2), which are in an
436 agreement with previous experiments (Irifune and Ringwood, 1993; Hirose, 2002; Iri-
437 fune et al., 2010; Ishii et al., 2018). The low temperature profiles for modern MORB
438 (hereafter referred to as ML) were obtained from the temperature model of the subduct-
439 ing model (Klein et al., 2017). The equilibrated temperature for modern MORB (ME)
440 was assumed to be same as the surrounding mantle (Brown and Shankland, 1981).

441 At 23–23.5 GPa, because of the post-spinel transition in pyrolite, the density dif-
442 ference between B30 and pyrolite drops by less than 0.1 g/cm^3 . The drop can be seen
443 in modern MORB but with a larger magnitude, 0.2 g/cm^3 . The proportions of Rw
444 in pyrolite is much smaller in the Archean than in the modern day (30 and 60 vol%,
445 respectively; Fig.S1), therefore the effect of the post-spinel transition on the density

446 increase is smaller in the Archean. The post-Gt transition in B30 and modern MORB
447 increases the density difference, but occurs at the different depths. The increase in the
448 density difference occurs at the lower pressures of 24.5–26 GPa in B30 than at 25–
449 29 GPa in modern MORB, depending on the temperature. If thermally equilibrated
450 with the surrounding mantle (i.e. AE or ME), the density difference of B30 becomes
451 negative only at 24–25 GPa (up to -0.03 g/cm^3), whereas that of modern MORB does
452 at 23.5–29 GPa (up to -0.09 g/cm^3). At the deeper depths, B30 maintains the positive
453 density difference by $0.1\text{--}0.2 \text{ g/cm}^3$ at the shallow depth than modern MORB does (26
454 and 29 GPa, respectively).

455 4.4. Density difference between subducting slabs and pyrolite

456 We calculated the density of the subducting slab by combining the densities of the
457 crust and harzburgite. The thicknesses of crust and harzburgite are 7 and 32 km for
458 the modern day and 40 and 74 km for the Archean. The detailed descriptions about
459 the density calculations for the subducting slab can be found in Text S2. The density
460 difference of the subducting slab with respect to pyrolite is shown as dashed lines in
461 Fig. 6.

462 In the Archean, subducting slabs are equal to or denser than pyrolite at most pres-
463 sures between 20–34 GPa (Fig. 6a). For the AL temperature, because of the post-spinel
464 transition in pyrolite, the density difference drops to -0.01 g/cm^3 at 23.3 GPa. For
465 the AE temperature, the drop in the density difference does not appear because of the
466 shallower depth of the post-spinel transition in Archean harzburgite at the higher slab
467 temperature (Text S2). Then, the cold slab maintains the greater density than pyrolite
468 above 28 GPa, while the thermally equilibrated slab becomes equally dense as pyrolite
469 at 29 GPa. On the other hand, the colder slabs are expected to be even denser than the
470 AL and AE slab cases because of the reduced volume at lower temperatures, therefore
471 the greater density difference with respect to pyrolite.

472 In the modern mantle, the density difference for the ML temperature is always
473 positive at 20–34 GPa (Fig. 6b). In contrast to the AL temperature, the ML temperature
474 does not show the large decrease in density difference at 23.3 GPa although the post-
475 spinel transition occurs at deeper depth in harzburgite of the slab than in pyrolite due

476 to the negative sign of the Clapeyron slope (Fig. S3). In the calculated model, the
477 temperature contrast of the slab along ML temperature with respect to pyrolite is not
478 large enough (~ 300 K; Text S2) to generate the noticeable difference in the depth of the
479 post-spinel transition between the slab and pyrolite. For even colder slabs in the modern
480 day, the marked decrease in the density difference is expected because of the larger
481 temperature contrast with respect to pyrolite, which will delay the post-spinel transition
482 in the slabs. For the ME temperature, the density difference becomes negative in 27.5–
483 29.6 GPa because of the persistent Gt in modern MORB at the higher slab temperature.
484 Above 30 GPa, the density difference for the ME slab becomes -0.01 g/cm³.

485 These results suggest that the contribution from the crustal density is much greater
486 in the Archean than in modern day because of the greater thickness of the crust in the
487 Archean slab (40 and 7 km-thick, respectively).

488 5. Discussion

489 5.1. *The density behaviors of the volcanic crust and subducting slab in the Archean*

490 We found that Archean volcanic crust (B30) is denser than the pyrolitic mantle at
491 the most depths of the lower MTZ and the shallow lower mantle regardless of the ther-
492 mal state of the crust, unlike modern MORB (Fig. 6). The different density behaviors
493 of the crust between in the Archean and in the modern day can be attributed to (1) the
494 effect of the Gt composition on the depth of the post-Gt transition in the crust and (2)
495 the temperature effect on the mineralogy of the pyrolitic mantle. First, both Archean
496 volcanic crust and modern MORB have Gt as the most abundant phase (~ 80 vol%) in
497 the mineralogy. The composition of Gt differs a lot between the two crusts (Table S2),
498 which may affect the depth of the post-Gt transition. For example, the Gt composi-
499 tion in Archean volcanic crust exhibits much smaller Al₂O₃ content than in modern
500 MORB (4.8 and 13.2 mol%, respectively; Table S2). The previous experiments (Ir-
501 ifune et al., 1996) suggested that the Al₂O₃ content may increase the stability of Gt
502 at higher pressure, which is consistent with our observations that Gt-out boundary in
503 Archean volcanic crust is at the shallower depth by 25–50 km-depth (1–2 GPa; Fig.3)
504 than that in the modern day. Second, the mineralogy of the pyrolitic mantle may be

505 different depending on temperature. Pyrolite shows only 30 vol% of Rw in the hotter
506 Archean, whereas 60 vol% of Rw in the cooler modern day (Fig. S1). The larger Rw
507 proportions in modern-day pyrolite results in the greater increase in the pyrolite den-
508 sity at 660 km-depth through the post-spinel transition. Therefore, the impact on the
509 decrease in the density difference of the crust with respect to the pyrolitic mantle might
510 be much larger in the modern day than in the Archean (Fig. 6).

511 Our density models of the subducting slab suggest that the effects on the net density
512 of the slab from the less dense harzburgite are smaller in the Archean than in the modern
513 day (Fig. 6). Rather, the greater density of Archean volcanic crust is more effective to
514 the net density of the slab owing to its larger portion in the slab (35 and 18% for
515 Archean volcanic crust and modern MORB, respectively; Table 1). As a result, the
516 density contrast between the subducting slab and the pyrolitic mantle is larger in the
517 Archean than in the modern day (Fig. 6).

518 *5.2. Previous studies on candidates for the subducted Archean volcanic rocks*

519 The exact composition of Archean volcanic crust remains uncertain (Herzberg
520 et al., 2010; Herzberg and Rudnick, 2012). Therefore, it is worthwhile to consider the
521 relevant compositions. The mineralogy and density of komatiite in the MTZ and the
522 topmost lower mantle have been documented by previous studies. Earlier experiments
523 by Nishihara and Takahashi (2001) studied Al-depleted komatiite with $(\text{Mg}+\text{Fe}+\text{Ca})/\text{Si}$
524 $= 1.38$ up to 23 GPa. They observed Gt and Rw at 19 GPa, consistent with our experi-
525 ments on B30 (Section 3.1). The Brg-in boundary is slightly shallower in Al-depleted
526 komatiite by 0.3 GPa than in B30, although their pressure calibration had a large uncer-
527 tainty at high pressure (Nishihara and Takahashi, 2001). At 21 GPa, Al-depleted ko-
528 matiite has a much larger proportion of Rw than B30 (40 and 14 vol%, respectively) be-
529 cause of the higher $(\text{Mg}+\text{Fe}+\text{Ca})/\text{Si}$ ratio. At 23 GPa, the stable phases of Al-depleted
530 komatiite are Gt + Brg + CaPv + Fp, consistent with B30 except that we did not find
531 Fp (Section 3.2) because of the lower MgO content in B30 (32.1 and 22.8 wt%, respec-
532 tively). They estimated the density of Al-depleted komatiite at high P - T through ther-
533 modynamic calculations based on the calculated zero-pressure densities of the phases
534 (Brown and Shankland, 1981). Their results showed the greater density of Al-depleted

535 komatiite than PREM density by 0.02–0.44 g/cm³ in the upper mantle and the MTZ.

536 Klein et al. (2017) proposed a model with a komatiitic composition with (Mg+Fe+Ca)/Si
537 = 1.12 that has less MgO than the one used in Nishihara and Takahashi (2001), but
538 similar to B30 in the present study (Table 1). In the thermally equilibrated slab, Gt
539 takes up to 92 vol% with minor CaPv and Fp at 20–23 GPa, but without Rw. Klein
540 et al. (2017) predicted the greater density of komatiite than the pyrolitic mantle in the
541 Archean except when thermally equilibrated. With the equilibrated temperature, the
542 komatiite density becomes smaller than pyrolite at 24–26 GPa, whereas the B30 den-
543 sity is always greater regardless of the slab temperature.

544 The general conclusions drawn from the previous studies on komatiite (Nishihara
545 and Takahashi, 2001; Klein et al., 2017) concur with this study on B30 in that the
546 greater density of Archean volcanic crust likely facilitates sinking of slabs into the
547 lower mantle.

548 5.3. *The sinking style of Archean volcanic crust and the scale of the mantle mixing*

549 Whether modern-style subduction occurred in the Archean is still under debate (e.g.
550 Van Hunen and Moyen, 2012; Tang et al., 2016; Condie, 2018). Other scenarios for
551 the material transportation into the deep interior in the Archean include the episodic-
552 style subduction (Van Hunen and Moyen, 2012), delamination (Johnson et al., 2014)
553 and shallow subduction (Foley et al., 2003). Van Hunen and Moyen (2012) showed
554 that the high temperature of the mantle would have weakened the harzburgite layer
555 of subducting slabs in the Archean, which would lead to the slab breaking. The fre-
556 quent break-off of the slabs could have resulted in the episodic-style subduction in the
557 Archean (Van Hunen and Moyen, 2012). The fragments of the slabs would lose some
558 of the driving forces of sinking, such as ridge-push and slab-pull, but we speculate that
559 the slab fragments would keep sinking because of the greater density of the slabs than
560 that of the surrounding mantle in the Archean. Johnson et al. (2014) suggested that
561 the base of Archean volcanic crust could have been gravitationally unstable due to the
562 local thickening, and eventually delaminated by Rayleigh-Taylor instabilities. The de-
563 laminated crust would sink because of the greater density than that of the surrounding
564 mantle (Klein et al., 2017). In addition, Foley et al. (2003) proposed that Archean crust

565 would have been recycled to the upper mantle through shallow subduction in the early
566 Archean. The subducting slabs may become stagnant in the upper mantle (Foley et al.,
567 2003). However, it is also possible that the stagnant slabs in the upper mantle break off
568 due to the hot mantle in the Archean (Van Hunen and Moyen, 2012) and sink into the
569 MTZ if the broken slabs are negatively buoyant in the upper mantle (Klein et al., 2017).
570 In any scenario, we speculate that in the Archean, the slabs or crusts would arrive to
571 the 670 km-discontinuity. Even though the slabs or crusts stagnate near the 670 km-
572 discontinuity, they would eventually descend into the lower mantle by Rayleigh-Taylor
573 instabilities.

574 Once modern-style global subduction had initiated, the volume of the material ex-
575 change between the MTZ and lower mantle might have increased. If the subduction
576 transported more materials into the lower mantle with modern-style global subduction,
577 the whole-mantle mixing might have become more efficient. In this case, the mantle
578 mixing with the redox heterogeneities from the lower mantle might have oxidized the
579 upper mantle, eventually leading to the rise of O₂ in the atmosphere toward the GOE
580 (Nicklas et al., 2019; Aulbach and Stagno, 2016; Andraut et al., 2018a).

581 *5.4. The time-dependent changes in the scale of material circulations in the mantle*

582 Since the onset of modern-style global subduction in the Archean (e.g., Laurent
583 et al., 2014; Tang et al., 2016; Condie, 2018), the composition of the subducted volcanic
584 crust have been changed with time. In this view, modern MORB and Archean volcanic
585 crust can represent the two end-members of the crustal compositions (Herzberg et al.,
586 2010; Johnson et al., 2014). As Earth's mantle cools, the composition of the volcanic
587 crust evolves toward the lower (Mg+Fe+Ca)/Si and more Al, and so does the compo-
588 sition of Gt. The change in the Gt composition might have deepen the depth of the
589 post-Gt transition with time. As a result, Gt becomes more stable at a deeper depth,
590 delaying the appearance of Brg, the high-density phase. Also, the thickness of the crust
591 in the slab becomes smaller, and therefore the density contribution from the crust be-
592 comes smaller. At the same time, the contribution from the harzburgitic layer becomes
593 greater for the net density of the subducting slab, if slab remains mechanically inte-
594 grated. As shown in Fig. 6, the subducting slab may have become less denser than the

595 surrounding mantle over time.

596 Today, seismic tomography images show different states of the modern subducting
597 slabs right beneath the MTZ. Slab stagnation is observed beneath the Western Pacific,
598 whereas subducting slabs seem to directly penetrate into the lower mantle beneath the
599 Central and South American subduction zones (e.g., van der Hilst and Seno, 1993;
600 Fukao et al., 2009; Li and McNamara, 2013; King et al., 2015). As discussed above, the
601 change in the composition and thickness of the crust over time might have reduced the
602 positive density contrast of the subducting slabs, which might partly contribute to the
603 slab stagnation. What we observe from the seismic tomography may be a snapshot of
604 the time-dependent transition of the style of the material circulations between the MTZ
605 and the lower mantle. Therefore, the scale of the mantle mixing may have changed
606 from single-layered since Archean to the two-layered in the future (Klein et al., 2017).

607 [Fig. 7]

608 *5.5. Archean materials in the present-day mantle*

609 The slow diffusion in the lower mantle (Holzapfel et al., 2005) may have allowed
610 Archean volcanic crust to survive until the present day. Such materials can contribute
611 to the seismic heterogeneities observed in the present-day mantle (Frost et al., 2017;
612 Wu et al., 2019). Particularly, a recent study raised a possibility of an accumulation of
613 ancient oceanic crust at 660 km-depth for the cause of small-scale seismic structures
614 (Wu et al., 2019). In order to evaluate the effect of density on the buoyancy of Archean
615 volcanic crust and Archean subducting slab in the pyrolitic modern mantle, we cal-
616 culated the densities of B30 and Archean harzburgite. The temperature for the crust
617 and slab was assumed to be the same as the surrounding mantle, therefore thermally
618 equilibrated (Brown and Shankland, 1981). The B30 density was obtained based on
619 the experimental data (Fig. 3), while those of Archean harzburgite and modern pyrolite
620 were calculated using Perple_X (Connolly, 2009) and the data set from Stixrude and
621 Lithgow-Bertelloni (2011). For Archean subducting slab, we assumed thicknesses of
622 40 and 74 km-thick for the crust and harzburgitic layer, respectively (Table 1).

623 We found that B30 remains denser than the pyrolitic mantle by 0.1 g/cm^3 through-
624 out at most depths between 580 and 900 km-depth (Fig. 7). If detached, the density

625 of Archean volcanic crust in the present-day mantle may prefer sinking into the lower
626 mantle to staying at 660 km-depth. In this case, the possible ancient oceanic crust at
627 660 km-depth that Wu et al. (2019) suggested is unlikely originated from Archean, but
628 more likely sometime close to the present day. For the case of the integrated slab, the
629 density of Archean slab appears to be the same as the modern mantle density at most
630 depths between 580 and 900 km-depth because the lower density of Archean harzburgite
631 cancels out the greater density of B30 (Fig. 7). Therefore, the density effect on the
632 buoyancy of Archean slab in the modern mantle at these depths may be negligible.

633 *5.6. Improving mineralogy modeling for Earth-like planets*

634 From the stellar elemental abundance, we can infer the bulk chemical compositions
635 of the exoplanets around the stars (Bond et al., 2010; Young et al., 2014; Unterborn and
636 Panero, 2017). Such studies have found a surprisingly large range of Mg/Si ratios for
637 the compositions. For the rocky exoplanets, Mg and Si are often assumed to exclu-
638 sively compose the mantle minerals. Therefore, in order to model the dynamics and
639 structures of the interior of the rocky exoplanets, it is important to have capability to
640 predict mineralogy from a range of different compositions. Because of the large param-
641 eteral space and the paucity of experimental data for such a large range of Mg/Si ratio,
642 thermodynamics codes, such as *Perple_X*, have become important tools to model the
643 mineralogy of the exoplanetary mantle (e.g. Dorn et al., 2015; Unterborn et al., 2017;
644 Vance et al., 2018).

645 Such thermodynamics codes have successfully reproduced the phase relations ob-
646 served in experiments for Earth's mantle-related compositions, such as pyrolite and
647 MORB, as also demonstrated in our modeling. Besides these two compositions, there
648 are little data at sufficiently high pressure to examine the predicted models through
649 comparison with experimental data. While the Mg/Si ratio of MORB (0.23; Gale et al.,
650 2013) is too low to be within the possible range of the Mg/Si ratio for Earth-like ex-
651 oplanets (e.g. 0.8–2 based on the stellar elemental abundances; Young et al., 2014),
652 that of pyrolite (e.g. Mg/Si=1.25; McDonough and Sun, 1995) can be useful to infer
653 the mantle mineralogy where Mg out-numbers Si (Mg/Si>1). Our new data on the B30
654 composition presented in this study provide the mineralogy with the sufficiently low

655 Mg/Si ratio (0.72), which is an important opportunity to test the modeling capability
656 for the large range of Mg/Si ratio for the possible mantle compositions.

657 Section 4.2 compares the mineralogy and the density between our experiments and
658 *Perple_X* model. While the density remains similar to each other at 20–34 GPa (Fig. 4),
659 the minor phases were additionally found in *Perple_X* model, partly because of the lack
660 of consideration of Fe^{3+} in the data set (Stixrude and Lithgow-Bertelloni, 2011). This
661 difference might be the reason for the different chemical compositions of the major
662 phase, such as Gt, which may in turn result in the different depths of the phase tran-
663 sition (24.8 and 28.1 GPa for the Gt-out boundary in our experiments and *Perple_X*
664 model, respectively). However, because the density and the major phase are similar be-
665 tween the experiments and *Perple_X* model for the other pressure ranges (20–24 GPa
666 and 28–34 GPa), we speculate these similarity may continue for the shallower mantle
667 and the deeper mantle. Gt is known to be stable throughout the upper mantle and the
668 MTZ (Irifune et al., 1996), while the Rw composition can exist in other forms of poly-
669 morphs, such as olivine and wadsleyite (Nishihara and Takahashi, 2001). In the lower
670 mantle, Brg and CaPv should persist up to ~ 100 GPa because of the large stability of
671 the perovskite structure (Irifune et al., 2010). Therefore, in spite of some differences in
672 the mineralogy and phase transition behaviors at 25–28 GPa, the use of *Perple_X* with
673 the data set from Stixrude and Lithgow-Bertelloni (2011) can be effective for modelling
674 the mantle mineralogy and density of Earth-like planets with the low Mg/Si ratio.

675 **6. Conclusion**

676 We have conducted experiments to investigate stable phases and density of Archean
677 volcanic crust in the pyrolitic mantle transition zone and lower mantle. Our experi-
678 ments showed that Archean volcanic crust is denser than the pyrolitic mantle regard-
679 less of temperature, increasing the likelihood of slab penetration across the lower MTZ
680 where modern MORB may experience the slab stagnation beneath some subduction
681 zones. We also modelled the density of the subducting slab in a combination of the
682 densities of the crust and the harzburgitic layer, with respect to the pyrolitic mantle
683 for both the Archean and modern day. The models predicted that the positive density

684 contrast between the subducting slab and the pyrolitic mantle is larger in the Archean
685 than in the modern day. Our results suggest that the density and the large thickness of
686 Archean volcanic crust would have promoted the further sinking into the lower mantle
687 in any tectonic styles. Therefore, the mantle mixing between the MTZ and the lower
688 mantle might have been efficient in the Archean.

689 **Acknowledgments**

690 We are grateful for helpful discussions with E. J. Garnero, M. Li, A. K. McNa-
691 mara, A. D. Anbar, S. J. Desch, C. Till, and R. L. Rudnick. K. Mossman and M.
692 R. Gutierrez assisted with the FIB and STEM measurements at Arizona State Uni-
693 versity (ASU). Y.-J. Chang and P. Wallace assisted with the FIB and STEM measure-
694 ments at University of Arizona. This study was supported by NSF EAR-1725094, the
695 Frontiers of Earth Systems Dynamics (FESD) program of NSF EAR-1135452, and
696 NASA NExSS grant NNX15AD53G (PI S. J. Desch). This work was also supported
697 by NSF (National Science Foundation) EAR-1725094. The portions of this work was
698 performed at GeoSoilEnviroCARS (The University of Chicago, Sector 13), Advanced
699 Photon Source (APS), Argonne National Laboratory. GeoSoilEnviroCARS is sup-
700 ported by NSF - Earth Sciences (EAR-1634415) and Department of Energy (DOE)
701 - GeoSciences (DE-FG02-94ER14466). Use of the COMPRES-GSECARS gas load-
702 ing system was supported by COMPRES under NSF Cooperative Agreement EAR-
703 1606856 and by GSECARS through NSF grant EAR-1634415 and DOE grant DE-
704 FG02-94ER14466. This research used resources of the APS, a U.S. DOE Office of
705 Science User Facility operated for the DOE Office of Science by Argonne National
706 Laboratory under Contract No. DE-AC02-06CH11357. This research used resources
707 of the Advanced Light Source, which is a DOE Office of Science User Facility under
708 contract no. DE-AC02-05CH11231. Beamline 12.2.2 is supported by COMPRES, the
709 Consortium for Materials Properties Research in Earth Sciences under NSF Coopera-
710 tive Agreement EAR 10-43050. The experimental data are provided as a run table in
711 supplementary material.

712 **References**

- 713 Andraut, D., Bolfan-Casanova, N., Guignot, N., 2001. Equation of state of lower
714 mantle (Al, Fe)-MgSiO₃ perovskite. *Earth and Planetary Science Letters* 193, 501–
715 508.
- 716 Andraut, D., Muñoz, M., Pesce, G., Cerantola, V., Chumakov, A., Kantor, I., Pas-
717 carelli, S., Rüffer, R., Hennet, L., 2018a. Large oxygen excess in the primitive man-
718 tle could be the source of the great oxygenation event. *Geochemical Perspectives*
719 *Letters* 6, 5–10.
- 720 Andraut, D., Pesce, G., Manthilake, G., Monteux, J., Bolfan-Casanova, N., Chantel,
721 J., Novella, D., Guignot, N., King, A., Itié, J.P., et al., 2018b. Deep and persistent
722 melt layer in the Archaean mantle. *Nature Geoscience* 11, 139.
- 723 Aulbach, S., Stagno, V., 2016. Evidence for a reducing Archean ambient mantle and
724 its effects on the carbon cycle. *Geology* 44, 751–754.
- 725 Baker, M.B., Beckett, J.R., 1999. The origin of abyssal peridotites: a reinterpretation
726 of constraints based on primary bulk compositions. *Earth and Planetary Science*
727 *Letters* 171, 49–61.
- 728 Bédard, J.H., 2006. A catalytic delamination-driven model for coupled genesis of Ar-
729 chaeen crust and sub-continental lithospheric mantle. *Geochimica et Cosmochimica*
730 *Acta* 70, 1188–1214.
- 731 Bond, J.C., O'Brien, D.P., Lauretta, D.S., 2010. The compositional diversity of ex-
732 trasolar terrestrial planets. I. In situ simulations. *The Astrophysical Journal* 715,
733 1050.
- 734 Brown, J., Shankland, T., 1981. Thermodynamic parameters in the earth as determined
735 from seismic profiles. *Geophysical Journal International* 66, 579–596.
- 736 Christensen, U.R., 1997. Influence of chemical buoyancy on the dynamics of
737 slabs in the transition zone. *Journal of Geophysical Research: Solid Earth* 102,

738 22435–22443. URL: [http://dx.doi.org/10.1029/](http://dx.doi.org/10.1029/97JB01342)
739 [97jb01342](http://dx.doi.org/10.1029/97JB01342), doi:10.1029/
740 [97jb01342](http://dx.doi.org/10.1029/97JB01342).

740 Condie, K.C., 2018. A planet in transition: The onset of plate tectonics on Earth
741 between 3 and 2 Ga? *Geoscience Frontiers* 9, 51–60.

742 Connolly, J., 2009. The geodynamic equation of state: what and how. *Geochemistry,*
743 *Geophysics, Geosystems* 10.

744 Davies, G.F., 2008. Episodic layering of the early mantle by the “basalt barrier” mech-
745 anism. *Earth and Planetary Science Letters* 275, 382–392. URL: [http://dx.doi.](http://dx.doi.org/10.1016/j.epsl.2008.08.036)
746 [org/10.1016/j.epsl.2008.08.036](http://dx.doi.org/10.1016/j.epsl.2008.08.036), doi:10.1016/j.epsl.2008.08.036.

747 Dorn, C., Khan, A., Heng, K., Connolly, J.A., Alibert, Y., Benz, W., Tackley, P., 2015.
748 Can we constrain the interior structure of rocky exoplanets from mass and radius
749 measurements? *Astronomy & Astrophysics* 577, A83.

750 Dorogokupets, P., Dewaele, A., 2007. Equations of state of MgO, Au, Pt, NaCl-B1,
751 and NaCl-B2: Internally consistent high-temperature pressure scales. *High Pressure*
752 *Research* 27, 431–446.

753 Foley, S.F., Buhre, S., Jacob, D.E., 2003. Evolution of the Archaean crust by delami-
754 nation and shallow subduction. *Nature* 421, 249.

755 Frost, D.A., Rost, S., Garnero, E.J., Li, M., 2017. Seismic evidence for Earth’s crusty
756 deep mantle. *Earth and Planetary Science Letters* 470, 54–63.

757 Frost, D.J., Liebske, C., Langenhorst, F., McCammon, C.A., Trønnes, R.G., Rubie,
758 D.C., 2004. Experimental evidence for the existence of iron-rich metal in the Earth’s
759 lower mantle. *Nature* 428, 409.

760 Fukao, Y., Obayashi, M., 2013. Subducted slabs stagnant above, penetrating through,
761 and trapped below the 660 km discontinuity. *Journal of Geophysical Research: Solid*
762 *Earth* 118, 5920–5938.

763 Fukao, Y., Obayashi, M., Nakakuki, T., Group, D.S.P., 2009. Stagnant slab: a review.
764 *Annual Review of Earth and Planetary Sciences* 37, 19–46.

765 Gale, A., Dalton, C.A., Langmuir, C.H., Su, Y., Schilling, J.G., 2013. The mean com-
766 position of ocean ridge basalts. *Geochemistry, Geophysics, Geosystems* 14, 489–
767 518.

768 Herzberg, C., Asimow, P.D., Arndt, N., Niu, Y., Lesher, C., Fitton, J., Cheadle, M.,
769 Saunders, A., 2007. Temperatures in ambient mantle and plumes: Constraints from
770 basalts, picrites, and komatiites. *Geochemistry, Geophysics, Geosystems* 8.

771 Herzberg, C., Condie, K., Korenaga, J., 2010. Thermal history of the Earth and its
772 petrological expression. *Earth and Planetary Science Letters* 292, 79–88.

773 Herzberg, C., Rudnick, R., 2012. Formation of cratonic lithosphere: An integrated
774 thermal and petrological model. *Lithos* 149, 4–15.

775 van der Hilst, R., Seno, T., 1993. Effects of relative plate motion on the deep structure
776 and penetration depth of slabs below the Izu-Bonin and Mariana island arcs. *Earth
777 and Planetary Science Letters* 120, 395–407.

778 Hirose, K., 2002. Phase transitions in pyrolitic mantle around 670-km depth: Impli-
779 cations for upwelling of plumes from the lower mantle. *Journal of Geophysical
780 Research: Solid Earth* 107.

781 Hirose, K., Fei, Y., 2002. Subsidius and melting phase relations of basaltic composi-
782 tion in the uppermost lower mantle. *Geochimica et Cosmochimica Acta* 66, 2099–
783 2108.

784 Hirose, K., Fei, Y., Ma, Y., Mao, H.K., 1999. The fate of subducted basaltic crust in
785 the Earth's lower mantle. *Nature* 397, 53.

786 Hirose, K., Takafuji, N., Sata, N., Ohishi, Y., 2005. Phase transition and density of
787 subducted MORB crust in the lower mantle. *Earth and Planetary Science Letters*
788 237, 239–251.

789 Holland, T., Redfern, S., 1997. UNITCELL: a nonlinear least-squares program for cell-
790 parameter refinement and implementing regression and deletion diagnostics. *Journal
791 of Applied Crystallography* 30, 84–84.

- 792 Holzapfel, C., Rubie, D.C., Frost, D.J., Langenhorst, F., 2005. Fe-Mg interdiffusion
793 in (Mg, Fe) SiO₃ perovskite and lower mantle reequilibration. *Science* 309, 1707–
794 1710.
- 795 Irifune, T., Koizumi, T., Ando, J.i., 1996. An experimental study of the garnet-
796 perovskite transformation in the system MgSiO₃-Mg₃Al₂Si₃O₁₂. *Physics of the*
797 *Earth and Planetary Interiors* 96, 147–157.
- 798 Irifune, T., Ringwood, A., 1993. Phase transformations in subducted oceanic crust and
799 buoyancy relationships at depths of 600–800 km in the mantle. *Earth and Planetary*
800 *Science Letters* 117, 101–110.
- 801 Irifune, T., Sekine, T., Ringwood, A., Hibberson, W., 1986. The eclogite-garnetite
802 transformation at high pressure and some geophysical implications. *Earth and Plan-*
803 *etary Science Letters* 77, 245–256.
- 804 Irifune, T., Shinmei, T., McCammon, C.A., Miyajima, N., Rubie, D.C., Frost, D.J.,
805 2010. Iron partitioning and density changes of pyrolite in Earth's lower mantle.
806 *Science* 327, 193–195.
- 807 Ishii, T., Huang, R., Fei, H., Koemets, I., Liu, Z., Maeda, F., Yuan, L., Wang, L.,
808 Druzhbin, D., Yamamoto, T., et al., 2018. Complete agreement of the post-spinel
809 transition with the 660-km seismic discontinuity. *Scientific reports* 8, 6358.
- 810 Ishii, T., Kojitani, H., Akaogi, M., 2011. Post-spinel transitions in pyrolite and
811 Mg₂SiO₄ and akimotoite–perovskite transition in MgSiO₃: precise comparison by
812 high-pressure high-temperature experiments with multi-sample cell technique. *Earth*
813 *and Planetary Science Letters* 309, 185–197.
- 814 Ito, Y., Toriumi, M., 2010. Silicon self-diffusion of MgSiO₃ perovskite by molecular
815 dynamics and its implication for lower mantle rheology. *Journal of Geophysical*
816 *Research: Solid Earth* 115.
- 817 Johnson, T.E., Brown, M., Kaus, B.J., VanTongeren, J.A., 2014. Delamination and
818 recycling of Archaean crust caused by gravitational instabilities. *Nature Geoscience*
819 7, 47.

- 820 Kasting, J.F., 2013. What caused the rise of atmospheric O₂? *Chemical Geology* 362,
821 13–25.
- 822 Katsura, T., Yamada, H., Shinmei, T., Kubo, A., Ono, S., Kanzaki, M., Yoneda, A.,
823 Walter, M.J., Ito, E., Urakawa, S., et al., 2003. Post-spinel transition in Mg₂SiO₄
824 determined by high *P–T* in situ X-ray diffractometry. *Physics of the Earth and*
825 *Planetary Interiors* 136, 11–24.
- 826 King, S.D., Frost, D.J., Rubie, D.C., 2015. Why cold slabs stagnate in the transition
827 zone. *Geology* 43, 231–234.
- 828 Klein, B.Z., Jagoutz, O., Behn, M.D., 2017. Archean crustal compositions pro-
829 mote full mantle convection. *Earth and Planetary Science Letters* 474, 516–526.
830 URL: <http://dx.doi.org/10.1016/j.epsl.2017.07.003>, doi:10.1016/j.
831 epsl.2017.07.003.
- 832 Korenaga, J., 2008. Urey ratio and the structure and evolution of Earth’s mantle. *Re-*
833 *views of Geophysics* 46.
- 834 Kubo, A., Akaogi, M., 2000. Post-garnet transitions in the system Mg₄Si₄O₁₂–
835 Mg₃Al₂Si₃O₁₂ up to 28 GPa: phase relations of garnet, ilmenite and perovskite.
836 *Physics of the Earth and Planetary Interiors* 121, 85–102.
- 837 Laurent, O., Martin, H., Moyen, J.F., Doucelance, R., 2014. The diversity and evolution
838 of late-Archean granitoids: Evidence for the onset of “modern-style” plate tectonics
839 between 3.0 and 2.5 Ga. *Lithos* 205, 208–235.
- 840 Letoullec, R., Pinceaux, J., Loubeyre, P., 1988. The membrane diamond anvil cell: a
841 new device for generating continuous pressure and temperature variations. *Interna-*
842 *tional Journal of High Pressure Research* 1, 77–90.
- 843 Li, M., McNamara, A.K., 2013. The difficulty for subducted oceanic crust to accumu-
844 late at the Earth’s core-mantle boundary. *Journal of Geophysical Research: Solid*
845 *Earth* 118, 1807–1816.

- 846 Litasov, K., Ohtani, E., Sano, A., Suzuki, A., Funakoshi, K., 2005. In situ X-ray
847 diffraction study of post-spinel transformation in a peridotite mantle: implication for
848 the 660-km discontinuity. *Earth and Planetary Science Letters* 238, 311–328.
- 849 Litasov, K., Ohtani, E., Suzuki, A., Kawazoe, T., Funakoshi, K., 2004. Absence of
850 density crossover between basalt and peridotite in the cold slabs passing through
851 660 km discontinuity. *Geophysical Research Letters* 31.
- 852 Litasov, K.D., Ohtani, E., 2005. Phase relations in hydrous MORB at 18–28GPa: im-
853 plications for heterogeneity of the lower mantle. *Physics of the Earth and Planetary*
854 *Interiors* 150, 239–263. URL: [http://dx.doi.org/10.1016/j.pepi.2004.](http://dx.doi.org/10.1016/j.pepi.2004.10.010)
855 [10.010](http://dx.doi.org/10.1016/j.pepi.2004.10.010), doi:10.1016/j.pepi.2004.10.010.
- 856 McCammon, C., 1997. Perovskite as a possible sink for ferric iron in the lower mantle.
857 *Nature* 387, 694.
- 858 McCammon, C., Ross, N., 2003. Crystal chemistry of ferric iron in (Mg, Fe)(Si, Al)
859 O₃ majorite with implications for the transition zone. *Physics and Chemistry of*
860 *Minerals* 30, 206–216.
- 861 McDonough, W.F., Sun, S.S., 1995. The composition of the Earth. *Chemical geology*
862 120, 223–253.
- 863 Nakagawa, T., Tackley, P.J., Deschamps, F., Connolly, J.A., 2010. The influence of
864 MORB and harzburgite composition on thermo-chemical mantle convection in a 3-d
865 spherical shell with self-consistently calculated mineral physics. *Earth and Planetary*
866 *Science Letters* 296, 403–412. URL: [http://dx.doi.org/10.1016/j.epsl.](http://dx.doi.org/10.1016/j.epsl.2010.05.026)
867 [2010.05.026](http://dx.doi.org/10.1016/j.epsl.2010.05.026), doi:10.1016/j.epsl.2010.05.026.
- 868 Newville, M., Stensitzki, T., Allen, D.B., Rawlik, M., Ingargiola, A., Nelson, A., 2016.
869 Lmfit: Non-linear least-square minimization and curve-fitting for python. *Astro-*
870 *physics Source Code Library* .
- 871 Nicklas, R.W., Puchtel, I.S., Ash, R.D., Piccoli, P.M., Hanski, E., Nisbet, E.G., Wa-
872 terton, P., Pearson, D.G., Anbar, A.D., 2019. Secular mantle oxidation across the

- 873 Archean-Proterozoic boundary: Evidence from V partitioning in komatiites and pi-
874 crites. *Geochimica et Cosmochimica Acta* .
- 875 Nishihara, Y., Takahashi, E., 2001. Phase relation and physical properties of an Al-
876 depleted komatiite to 23 GPa. *Earth and Planetary Science Letters* 190, 65–77.
- 877 Ogawa, M., 2003. Chemical stratification in a two-dimensional convecting mantle
878 with magmatism and moving plates. *Journal of Geophysical Research* 108. URL:
879 <http://dx.doi.org/10.1029/2002JB002205>, doi:10.1029/2002jb002205.
- 880 Oguri, K., Funamori, N., Uchida, T., Miyajima, N., Yagi, T., Fujino, K., 2000. Post-
881 garnet transition in a natural pyrope: a multi-anvil study based on in situ X-ray
882 diffraction and transmission electron microscopy. *Physics of the Earth and Planetary*
883 *Interiors* 122, 175–186.
- 884 Palin, R.M., White, R.W., 2016. Emergence of blueschists on Earth linked to secular
885 changes in oceanic crust composition. *Nature Geoscience* 9, 60.
- 886 Prakapenka, V., Kubo, A., Kuznetsov, A., Laskin, A., Shkurikhin, O., Dera, P., Rivers,
887 M., Sutton, S., 2008. Advanced flat top laser heating system for high pressure re-
888 search at GSECARS: application to the melting behavior of germanium. *High Pres-*
889 *sure Research* 28, 225–235.
- 890 Prescher, C., Prakapenka, V.B., 2015. DIOPTAS: a program for reduc-
891 tion of two-dimensional X-ray diffraction data and data exploration.
892 *High Pressure Research* 35, 223–230. URL: [http://dx.doi.org/10.](http://dx.doi.org/10.1080/08957959.2015.1059835)
893 [1080/08957959.2015.1059835](http://dx.doi.org/10.1080/08957959.2015.1059835), doi:10.1080/08957959.2015.1059835,
894 [arXiv:http://dx.doi.org/10.1080/08957959.2015.1059835](http://dx.doi.org/10.1080/08957959.2015.1059835).
- 895 Ricolleau, A., Perrillat, J.p., Fiquet, G., Daniel, I., Matas, J., Addad, A., Menguy, N.,
896 Cardon, H., Mezouar, M., Guignot, N., 2010. Phase relations and equation of state
897 of a natural MORB: Implications for the density profile of subducted oceanic crust
898 in the Earth's lower mantle. *Journal of Geophysical Research: Solid Earth* 115.
- 899 Ringwood, A.E., Irifune, T., 1988. Nature of the 650-km seismic discontinuity: impli-
900 cations for mantle dynamics and differentiation. *Nature* 331, 131.

- 901 Rivers, M., Prakapenka, V.B., Kubo, A., Pullins, C., Holl, C.M., Jacobsen, S.D., 2008.
902 The COMPRES/GSECARS gas-loading system for diamond anvil cells at the Ad-
903 vanced Photon Source. *High Pressure Research* 28, 273–292.
- 904 Schulz, K., 1982. Magnesian basalts from the Archaean terrains of Minnesota. Ko-
905 matiites. London, George Allen & Unwin , 171–186.
- 906 Shim, S.H., 2017a. PeakPo - a python software for X-ray diffraction analysis at
907 high pressure and high temperature. URL: [https://doi.org/10.5281/zenodo.](https://doi.org/10.5281/zenodo.842949)
908 842949, doi:10.5281/zenodo.842949.
- 909 Shim, S.H., 2017b. Pytheos - a python tool set for equations of state pytheos - a
910 python tool set for equations of state. URL: [https://doi.org/10.5281/zenodo.](https://doi.org/10.5281/zenodo.802392)
911 802392, doi:10.5281/zenodo.802392.
- 912 Shim, S.H., Grocholski, B., Ye, Y., Alp, E.E., Xu, S., Morgan, D., Meng, Y.,
913 Prakapenka, V.B., 2017. Stability of ferrous-iron-rich bridgmanite under reducing
914 midmantle conditions. *Proceedings of the National Academy of Sciences* 114, 6468–
915 6473.
- 916 Sinmyo, R., Hirose, K., 2010. The soret diffusion in laser-heated diamond-anvil cell.
917 *Physics of the Earth and Planetary Interiors* 180, 172–178.
- 918 Speziale, S., Lee, V., Clark, S., Lin, J., Pasternak, M., Jeanloz, R., 2007. Effects of
919 fe spin transition on the elasticity of (Mg, Fe) O magnesiowüstites and implications
920 for the seismological properties of the Earth's lower mantle. *Journal of Geophysical*
921 *Research: Solid Earth* 112.
- 922 Stixrude, L., Lithgow-Bertelloni, C., 2005. Thermodynamics of mantle minerals—I.
923 physical properties. *Geophysical Journal International* 162, 610–632.
- 924 Stixrude, L., Lithgow-Bertelloni, C., 2011. Thermodynamics of mantle minerals-II.
925 phase equilibria. *Geophysical Journal International* 184, 1180–1213.
- 926 Stixrude, L., Lithgow-Bertelloni, C., 2012. Geophysics of chemical heterogeneity in
927 the mantle. *Annual Review of Earth and Planetary Sciences* 40, 569–595.

- 928 Tang, M., Chen, K., Rudnick, R.L., 2016. Archean upper crust transition from mafic
929 to felsic marks the onset of plate tectonics. *Science* 351, 372–375.
- 930 Tangeman, J.A., Phillips, B.L., Navrotsky, A., Weber, J., Hixson, A.D., Key, T.S.,
931 2001. Vitreous forsterite (Mg_2SiO_4): synthesis, structure, and thermochemistry.
932 *Geophysical research letters* 28, 2517–2520.
- 933 Toby, B.H., Von Dreele, R.B., 2013. GSAS-II: the genesis of a modern open-source all
934 purpose crystallography software package. *Journal of Applied Crystallography* 46,
935 544–549.
- 936 Unterborn, C.T., Desch, S.J., Hinkel, N.R., Lorenzo Jr, A., 2017. Inward migration
937 of the TRAPPIST-1 planets as inferred from their water-rich compositions. *arXiv*
938 preprint arXiv:1706.02689 .
- 939 Unterborn, C.T., Panero, W.R., 2017. The effects of Mg/Si on the exoplanetary refrac-
940 tory oxygen budget. *The Astrophysical Journal* 845, 61.
- 941 Van Hunen, J., Moyen, J.F., 2012. Archean subduction: fact or fiction? *Annual Review*
942 *of Earth and Planetary Sciences* 40, 195–219.
- 943 Vance, S.D., Panning, M.P., Stähler, S., Cammarano, F., Bills, B.G., Tobie, G., Ka-
944 mata, S., Kedar, S., Sotin, C., Pike, W.T., et al., 2018. Geophysical investigations of
945 habitability in ice-covered ocean worlds. *Journal of Geophysical Research: Planets*
946 123, 180–205.
- 947 Wu, W., Ni, S., Irving, J.C., 2019. Inferring Earth’s discontinuous chemical layering
948 from the 660-kilometer boundary topography. *Science* 363, 736–740.
- 949 Xu, J., Yamazaki, D., Katsura, T., Wu, X., Remmert, P., Yurimoto, H., Chakraborty,
950 S., 2011. Silicon and magnesium diffusion in a single crystal of MgSiO_3 perovskite.
951 *Journal of Geophysical Research: Solid Earth* 116.
- 952 Xu, W., Lithgow-Bertelloni, C., Stixrude, L., Ritsema, J., 2008. The effect of bulk com-
953 position and temperature on mantle seismic structure. *Earth and Planetary Science*
954 *Letters* 275, 70–79.

- 955 Ye, Y., Gu, C., Shim, S.H., Meng, Y., Prakapenka, V., 2014. The postspinel boundary
956 in pyrolitic compositions determined in the laser-heated diamond anvil cell. *Geo-*
957 *physical Research Letters* 41, 3833–3841.
- 958 Ye, Y., Prakapenka, V., Meng, Y., Shim, S.H., 2017. Intercomparison of the gold, plat-
959 inum, and MgO pressure scales up to 140 GPa and 2500 K. *Journal of Geophysical*
960 *Research: Solid Earth* 122, 3450–3464.
- 961 Young, P.A., Desch, S.J., Anbar, A.D., Barnes, R., Hinkel, N.R., Kopparapu, R., Mad-
962 husudhan, N., Monga, N., Pagano, M.D., Riner, M.A., et al., 2014. Astrobiological
963 stoichiometry. *Astrobiology* 14, 603–626.

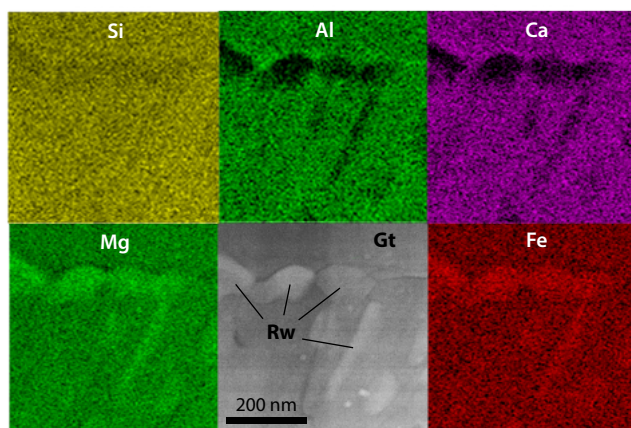


Figure 1: A high-angle annular dark-field image in the different region with chemical maps of B30 in LH-DAC. The sample was synthesized at 19.5 GPa and 1,900 K. The brighter color in each chemical map represents the more concentration of the corresponding element. The chemical compositions and the proportions of individual phases are provided in Table 2. Gt: garnet; Rw: ringwoodite.

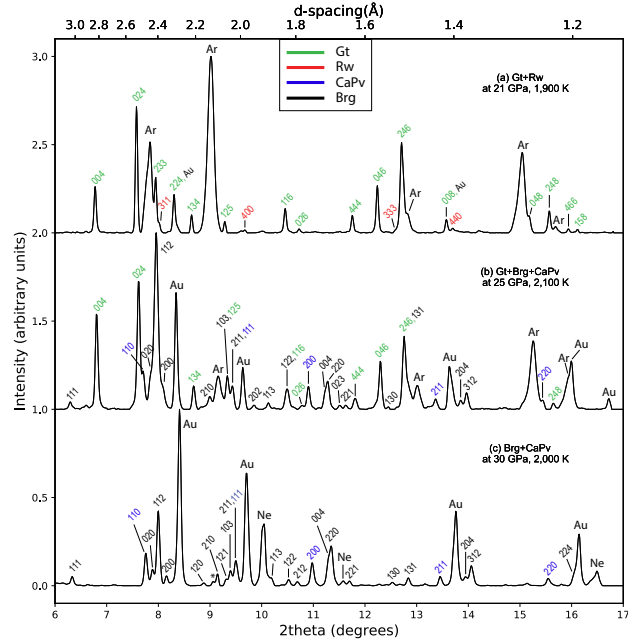


Figure 2: In-situ X-ray diffraction (XRD) patterns of B30 at high P - T in laser-heated diamond anvil cell (LHDAC). X-ray energy was 37 keV. We provided the Miller indices of the major lines. Gt: garnet; Rw: ringwoodite; CaPv: CaSiO_3 perovskite; Brg: bridgmanite; Au: gold (pressure standard); Ar: argon (medium); Ne: Neon (medium); and *: unidentified peaks.

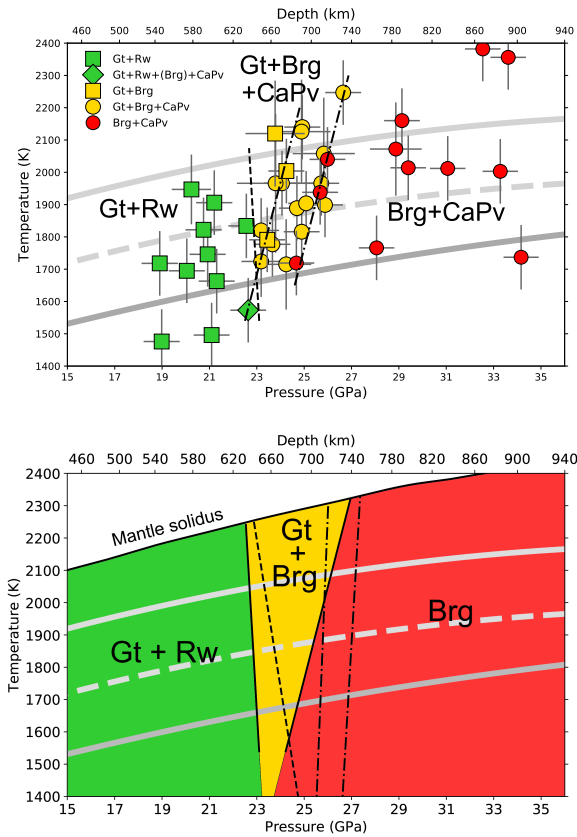


Figure 3: Phase changes in the B30 composition at high pressure and temperature. The light gray line represents the Archean mantle geotherm, which was shifted by 200 K from the modern mantle geotherm (the dashed gray line; Brown and Shankland, 1981). The gray line represent the temperature profile of the subducting slab after Klein et al. (2017). Top: Each symbol represents one heating cycle in the LHDAC experiments. The dashed and dot-dashed lines indicate the post-spinel and post-Gt transition boundaries determined in this study, respectively. Bottom: The major phases in the distinctive mineralogy fields. The black solid lines are Brg-in and Gt-out boundaries determined in this study. The Brg-in boundary of the post-spinel transition in pyrolite (Hirose, 2002) is plotted as the dashed line. The Brg-in (left) and Gt-out (right) boundaries in modern MORB (Hirose et al., 1999) are plotted as the dot-dashed lines. The mantle solidus is obtained from Andraut et al. (2018b). Gt: garnet; Rw: ringwoodite; CaPv: calcium perovskite; Brg: bridgmanite.

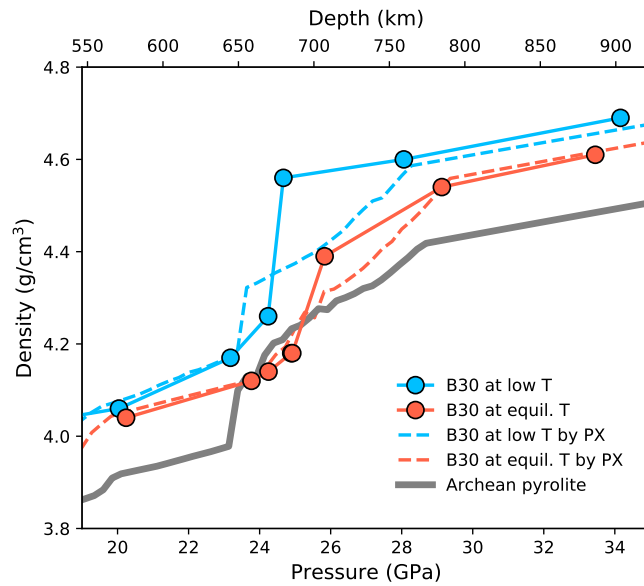


Figure 4: Density of B30 along different temperature profiles in the Archean. The orange, and red curves represent low (AL), and equilibrated (AE) temperature profiles in the Archean, respectively. The solid and dashed lines indicate densities determined by experiments and by Perple_X (PX; Connolly, 2009), respectively. The circles along the solid lines represent the data points obtained from our experiments. Information on the temperature profiles can be found in Table S3.

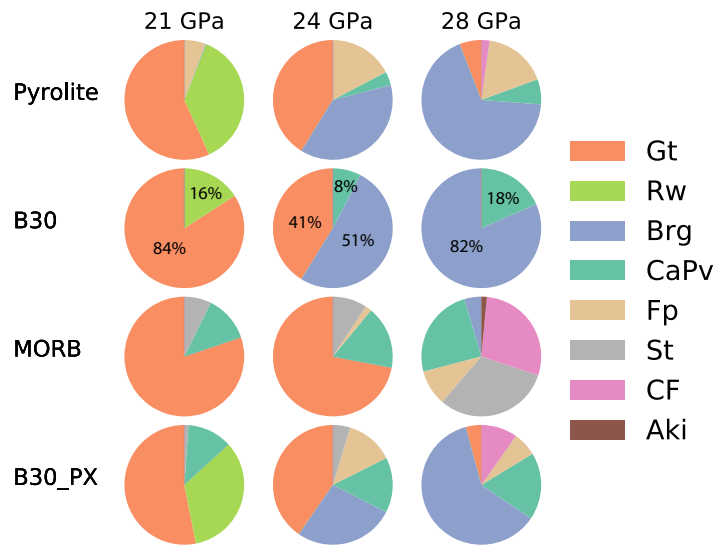


Figure 5: The mineralogy for pyrolite, B30, MORB in vol% in the MTZ and the topmost lower mantle. The mineralogy of B30 is from the experimental results in this study. Mineralogies of pyrolite, MORB, and B30_PX were calculated using Perple_X (Connolly, 2009) and the data set from Stixrude and Lithgow-Bertelloni (2011). Gt: garnet; Rw: ringwoodite; Brg: bridgmanite; CaPv: CaSiO₃ perovskite; Fp: ferropericlase; St: stishovite; CF: calcium ferrite; Aki: Akimotoite.

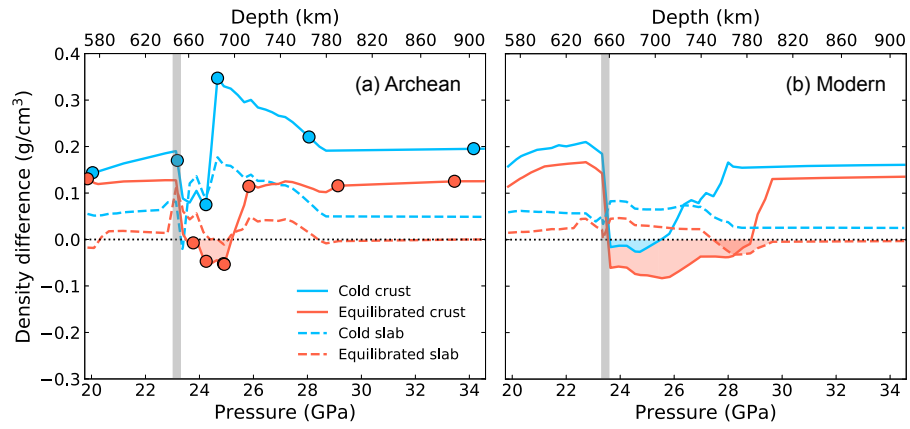


Figure 6: Density differences of the crusts and subducting slabs with respect to the pyrolytic mantle: (a) B30 and subducting slab in the Archean and (b) MORB and subducting slab in the modern day. The open circles in (a) represent the experimental data points from this study. The vertical gray bars indicate the depth of the post-spinel transition in the pyrolytic mantle. The depths of the negative density contrast are shaded. For subducting slabs, the thicknesses of crust and harzburgite are 40 and 74 km for the Archean, and 7 and 32 km for the modern day, respectively (Text S2). Information on the temperature profiles can be found in Table S3.

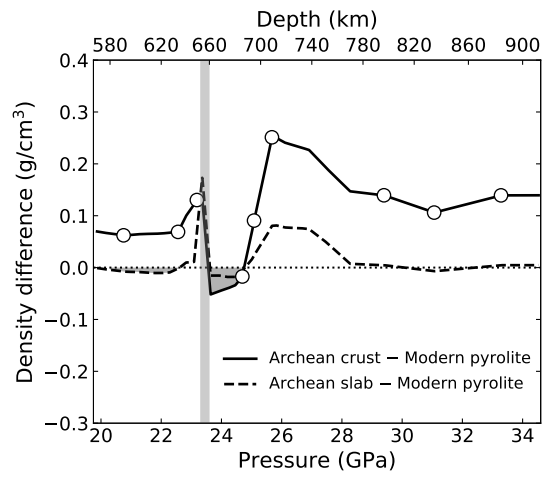


Figure 7: The density differences of B30 and Archean subducting slab with respect to the pyrolitic mantle in the modern day. The open circles represent our experimental data. The temperatures of B30 and Archean harzburgite were assumed to be equilibrated to modern mantle (Brown and Shankland, 1981)). The depth of the post-spinel transition in pyrolite is marked as the vertical grey bar. The densities of Archean harzburgite and pyrolite were calculated using *Perple_X* (Connolly, 2009) and the data set from Stixrude and Lithgow-Bertelloni (2011).

Table 1: Chemical compositions of pyrolite, basaltic crust, complementary residues, and Archean volcanic crust. After excluding minor elements, we normalized each composition to 100%.

wt%	Pyrolite ^a	B30 ^b	Modern MORB ^c	Archean residue ^b	Modern residue ^d	Archean crust ^e
SiO ₂	45.1	47.0	51.8	43.8	43.4	47.6
Al ₂ O ₃	4.8	7.5	15.5	2.8	1.3	7.1
FeO [†]	8.4	12.7	10.1	6.4	8.6	12.3
MgO	37.7	22.8	8.0	46.3	45.7	22.9
CaO	3.5	8.8	11.7	0.8	0.9	8.3
Na ₂ O	0.4	1.3	2.1	0	0	1.7
Mg# [‡]	88.9	76.2	58.5	92.8	90.4	76.8
(Mg+Fe+Ca)/Si	1.49	1.15	0.63	1.72	1.76	1.12
Thickness (km) [§]	-	40	7	74	32	-

^a Composition obtained from McDonough and Sun (1995)

^b Modeled compositions obtained from Johnson et al. (2014). B30 was used for experiments in this study.

^c Composition obtained from Gale et al. (2013)

^d Composition obtained from Baker and Beckett (1999)

^e Oceanic plateau basalt 3.3 Ga; Schulz (1982)

† All Fe in B30 is assumed to exist as FeO.

‡ Mg# = Mg/(Mg+Fe)

§ Thickness of a layer in the subducting slab considered in this study.

Table 2: Chemical compositions of the recovered samples from the Gt-dominant P - T field and the Brg-dominant P - T field. The compositions were normalized to be 100% in total.

wt%	19.5 GPa [†] , 1,900 K		31 GPa, 2,000 K	
	Gt	Rw	Brg	CaPv
SiO ₂	49.7	41.4	47.9	48.1
Al ₂ O ₃	8.6	2.7	9.0	1.1
FeO ^a	11.8	23.8	13.1	4.6
MgO	20.9	29.2	26.3	3.4
CaO	9.0	2.8	3.7	42.8
Proportions (vol%)				
Mass balance	82.7	17.3	81.6	18.4
EDS mapping	85.3	14.7		
Rietveld	85.5	14.5	82.2	17.8
Average ^b (vol%)	84.5	15.5	81.9	18.1

^aAll Fe is assumed to be Fe²⁺.

^bAveraged proportions from the two different methods.

[†]Pressure was measured at 300 K.

Supplementary material for “Mineralogy and Density of Archean Volcanic Crust in the Mantle Transition Zone”

Byeongkwan Ko^{a,*}, Vitali Prakapenka^b, Martin Kunz^c, Clemens Prescher^{b,d},
Kurt Leinenweber^a, Sang-Heon Shim^{a,*}

^a*School of Earth and Space Exploration, Arizona State University, Tempe, Arizona 85287,
United States*

^b*Center for Advanced Radiation Sources, University of Chicago, Chicago, Illinois 60439,
United States*

^c*Advanced Light Source, Lawrence Berkeley National Laboratory, Berkeley, California
94720, United States*

^d*Now at Photon Sciences, Deutsches Elektronen-Synchrotron (DESY), Hamburg 22607,
Germany*

Contents of this file

1. Text S1 to S2
 2. Figures S1 to S3
 3. Tables S1 to S3
-
-

Introduction

This supplementary material provides the texts, figures and tables to support the main article. The texts includes the further explanations for the density models used in this study and the descriptions of the harzburgite density. The figures include the phase diagrams, the plot of temperature gradients, and the harzburgite density. The tables provide details of experimental conditions and results.

*Corresponding author

Email addresses: byeongkw@asu.edu (Byeongkwan Ko), SHDShim@gmail.com (Sang-Heon Shim)

964 **Text S1. The density model for the Gt-Brg transition P - T field**

965 In our model for density calculation in Gt-Brg transition P - T field, we as-
966 sume that Rw transforms univariantly to Brg + Fp at the Brg-in boundary, and
967 that Gt transforms gradually to Brg + CaPv over a pressure interval. We as-
968 sume that Fp exists together with Gt and Brg although we did not observe Fp in
969 XRD patterns. The phase proportions for the Gt+Brg+Fp mineralogy were de-
970 termined by converting Rw proportion to Brg and Fp, whose compositions were
971 passed down from the measured Rw composition (run #4430; Table 2). We cal-
972 culated the molar volume of Fp using the equation of state of $Mg_{0.83}Fe_{0.17}$ from
973 Speziale et al. (2007). For the Gt+Brg+CaPv mineralogy, the gradual trans-
974 formation of Gt to Brg and CaPv was considered along the slab temperatures
975 between CaPv-in boundary and Gt-out boundary. At CaPv-in boundary, the
976 number of mols of Gt is $X_{Gt}=1$, which decreases linearly by breaking down into
977 Brg and CaPv until Gt is all consumed ($X_{Gt}=0$) at Gt-out boundary. With the
978 fixed chemical composition of Gt (Table 2), we estimated the number of mols
979 of Brg (X_{Brg}) and CaPv (X_{CaPv}) formed by the breakdown of Gt ($1 \text{ mol}_{Gt} =$
980 $3.3 \text{ mols}_{Brg} + 0.7 \text{ mols}_{CaPv}$). On the other hand, we assumed that Fp does not
981 exist in the Gt+Brg+CaPv mineralogy because of the disproportionation reac-
982 tion of Brg (Frost et al., 2004). In this way, we predicted the phase proportions
983 at the Gt-out boundary to be 85.7, and 14.3 mol% for Brg and CaPv, respec-
984 tively, consistent well with the phase proportions determined by mass balance
985 and Rietveld refinement for the Brg-dominant mineralogy (run #218; Table 2).

986 **Text S2. Density difference of harzburgite in the Archean and modern**
987 **day**

988 Ringwood (1982) proposed a model for the petrological structure of the
989 oceanic lithosphere that is composed mainly of the basaltic crust, harzburgitic,
990 and lherzolitic (depleted pyrolite) lithospheres. The density of the lherzolitic
991 lithosphere should be greater than or at least the same as the surrounding
992 mantle because of the same chemical composition but in the lower temperature
993 or the equilibrated temperature, respectively. Therefore, for the case of the
994 subducting slab the chemical effects on the density of the subducting slab is
995 primarily governed by the harzburgitic lithosphere as well as the crust (Klein
996 et al., 2017; Irifune and Ringwood, 1987).

997 When the volcanic crust forms from partial melting of the mantle, it will cre-
998 ate complementary residue (harzburgite) beneath the crustal layer. Therefore,
999 the crust and complementary harzburgite have compositional relations with re-
1000 spect to the undepleted mantle (pyrolite). Such relations allow us to estimate
1001 the thickness of harzburgitic layer. If we assume their volumes are linearly pro-
1002 portional to their thicknesses, we can describe an equation as follows (Xu et al.,
1003 2008):

$$H_{Crust}X_{Crust} + H_{Harz}X_{Harz} = (H_{Crust} + H_{Harz})X_{Pyro} \quad (S1)$$

1004 where X_{Crust} , X_{Harz} , and X_{Pyro} are the compositions of the crust, comple-
1005 mentary harzburgite, and pyrolite, respectively and H_{Crust} and H_{Harz} are the
1006 thicknesses of the crust and complementary harzburgite, respectively. With
1007 the given thickness of the crust and the compositions of the crust and com-
1008plementary harzburgite, we can determine the thickness of the complementary
1009 harzburgite using the following equation:

$$H_{Harz} = H_{Crust} \frac{X_{Pyro} - X_{Crust}}{X_{Harz} - X_{Pyro}} \quad (S2)$$

1010 In our study, we used thicknesses of 7 and 40 km for the modern and Archean
1011 crusts (i.e. modern MORB and B30), respectively, which yield thicknesses of

1012 32 and 74 km for the modern and Archean complementary harzburgites, re-
1013 spectively (Table 1). We used *Perple_X* to calculate the density of Archean
1014 harzburgite. Although Archean harzburgite has not been cross-examined by
1015 both the experiments and *Perple_X*, unlike the modern harzburgite (Irifune and
1016 Ringwood, 1987; Stixrude and Lithgow-Bertelloni, 2012; Xu et al., 2008), its
1017 composition remains very similar to modern harzburgite composition (Table 1).
1018 Therefore, Archean harzburgite is expected to yield nearly the same mineralogy
1019 as modern harzburgite (Fig. S1).

1020 The density difference between harzburgite and pyrolite in the Archean and
1021 modern day is shown in Fig. S3. The calculated mineralogy of harzburgite is
1022 nearly the same in between the Archean and modern day (Fig. S1) because
1023 of the similar chemical compositions (Table 1). At 20–23.5 GPa, *Rw* is dom-
1024 inant (80–90 vol%), while *Gt* represents 10–19 vol% in harzburgite, depending
1025 on temperature. Above 23.5 GPa, *Brg* becomes the most abundant phase and
1026 its proportion increases by the post-*Gt* transition (70–75 vol%) up to 25.9 and
1027 27.5 GPa, for both Archean and modern harzburgites, respectively (Fig. S1).

1028 The density difference of Archean harzburgite with respect to pyrolite changes
1029 with the temperature profile. The AL and AE temperatures have lower den-
1030 sities than pyrolite (Fig. S3) except for 23–28 GPa. For the AL temperature,
1031 the density difference decreases at ~ 23.3 GPa due to the post-spinel transition
1032 in pyrolite, followed by a sharp increase at ~ 24 GPa because of the post-spinel
1033 transition in Archean harzburgite. For the AE temperature, the density differ-
1034 ence abruptly increases at 23 GPa, because of the post-spinel transition which
1035 occurs at the same depth in Archean harzburgite and pyrolite. Archean harzbur-
1036 gite forms the larger amount of *Brg* at 23 GPa than pyrolite (53 and 23.54 vol%,
1037 respectively) because of the larger amount of *Rw* (76 and 34 vol%, respectively),
1038 leading the steep increase without the sudden drop in density difference.

1039 Above 24 GPa, Archean harzburgite shows a gradual decrease in the density
1040 difference because of the gradual post-*Gt* transition in pyrolite until 28.5 GPa.
1041 Above 28.5 GPa, Archean harzburgite becomes less dense than pyrolite up to
1042 34 GPa for the AL and AE temperatures, respectively.

1043 Compared to Archean harzburgite, modern harzburgite shows very similar
1044 trend in the density difference, but with the systemically greater density. The
1045 greater density of modern harzburgite may largely be the lower temperature in
1046 the modern day than in the Archean. At 23.8 GPa, both the ML and ME tem-
1047 peratures show the marginal decrease (0.01-0.02 g/cm³) in the density difference
1048 of modern harzburgite. Although the transition depth of modern harzburgite
1049 becomes deeper with the lower temperature (ML) because of the negative sign
1050 of the Clapeyron slope of the post-spinel transition, the difference in the depth
1051 of the post-spinel transition between the slab and pyrolite is relatively small.
1052 This is because the temperature contrast between the slab along the ML tem-
1053 perature and pyrolite is smaller in the modern day than in the Archean (~300
1054 and ~400 K, respectively). Therefore, the difference in the depth of the post-
1055 spinel transition with respect to pyrolite becomes smaller in the modern day.
1056 Modern harzburgite along the ML temperature does not show the sudden drop
1057 of the density difference at 23.8 GPa, unlike Archean harzburgite with the AL
1058 temperature.

1059 **References**

- 1060 Brown, J., Shankland, T., 1981. Thermodynamic parameters in the earth as
1061 determined from seismic profiles. *Geophysical Journal International* 66, 579–
1062 596.
- 1063 Connolly, J., 2009. The geodynamic equation of state: what and how. *Geo-*
1064 *chemistry, Geophysics, Geosystems* 10.
- 1065 Dorogokupets, P., Dewaele, A., 2007. Equations of state of MgO, Au, Pt, NaCl-
1066 B1, and NaCl-B2: Internally consistent high-temperature pressure scales.
1067 *High Pressure Research* 27, 431–446.
- 1068 Frost, D.J., Liebske, C., Langenhorst, F., McCammon, C.A., Trønnnes, R.G.,
1069 Rubie, D.C., 2004. Experimental evidence for the existence of iron-rich metal
1070 in the Earth’s lower mantle. *Nature* 428, 409.
- 1071 Hirose, K., 2002. Phase transitions in pyrolitic mantle around 670-km depth:
1072 Implications for upwelling of plumes from the lower mantle. *Journal of Geo-*
1073 *physical Research: Solid Earth* 107.
- 1074 Hirose, K., Fei, Y., 2002. Subsolidus and melting phase relations of basaltic
1075 composition in the uppermostlower mantle. *Geochimica et Cosmochimica*
1076 *Acta* 66, 2099–2108.
- 1077 Irifune, T., Ringwood, A., 1987. Phase transformations in a harzburgite com-
1078 position to 26 GPa: implications for dynamical behaviour of the subducting
1079 slab. *Earth and Planetary Science Letters* 86, 365–376.
- 1080 Klein, B.Z., Jagoutz, O., Behn, M.D., 2017. Archean crustal compositions
1081 promote full mantle convection. *Earth and Planetary Science Letters* 474,
1082 516–526. URL: <http://dx.doi.org/10.1016/j.epsl.2017.07.003>, doi:10.
1083 1016/j.epsl.2017.07.003.
- 1084 Ringwood, A.E., 1982. Phase transformations and differentiation in sub-
1085 ducted lithosphere: implications for mantle dynamics, basalt petrogenesis,
1086 and crustal evolution. *The Journal of Geology* 90, 611–643.

- 1087 Speziale, S., Lee, V., Clark, S., Lin, J., Pasternak, M., Jeanloz, R., 2007. Ef-
1088 fects of fe spin transition on the elasticity of (Mg, Fe) O magnesiowüstites
1089 and implications for the seismological properties of the Earth's lower mantle.
1090 Journal of Geophysical Research: Solid Earth 112.
- 1091 Stixrude, L., Lithgow-Bertelloni, C., 2011. Thermodynamics of mantle minerals-
1092 II. phase equilibria. Geophysical Journal International 184, 1180–1213.
- 1093 Stixrude, L., Lithgow-Bertelloni, C., 2012. Geophysics of chemical heterogeneity
1094 in the mantle. Annual Review of Earth and Planetary Sciences 40, 569–595.
- 1095 Xu, W., Lithgow-Bertelloni, C., Stixrude, L., Ritsema, J., 2008. The effect of
1096 bulk composition and temperature on mantle seismic structure. Earth and
1097 Planetary Science Letters 275, 70–79.
- 1098 Ye, Y., Prakapenka, V., Meng, Y., Shim, S.H., 2017. Intercomparison of the
1099 gold, platinum, and MgO pressure scales up to 140 GPa and 2500 K. Journal
1100 of Geophysical Research: Solid Earth 122, 3450–3464.

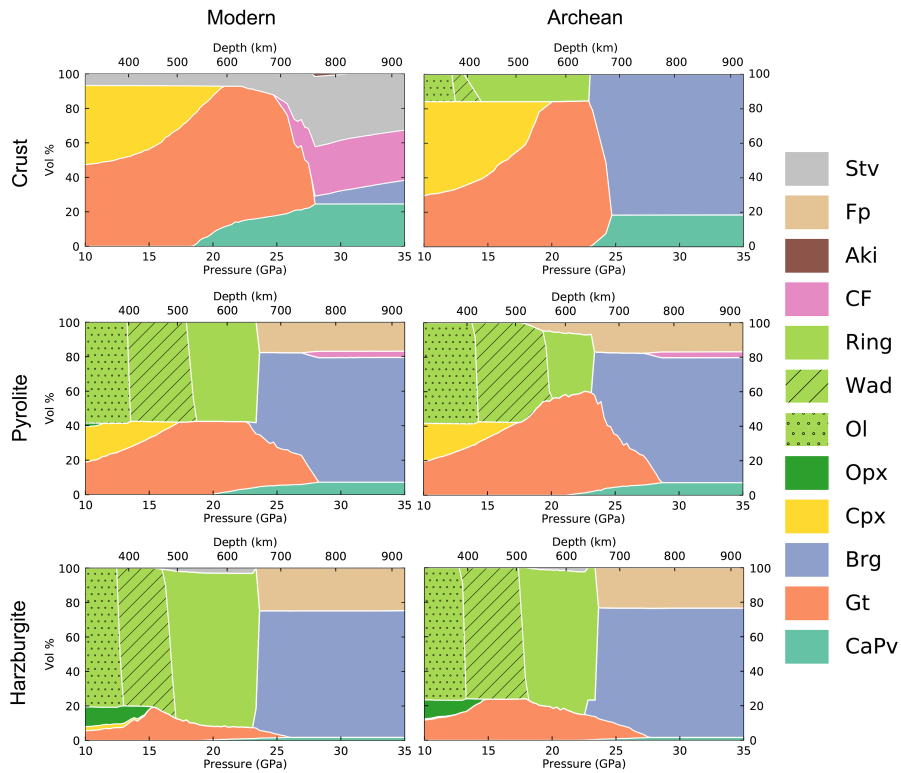


Figure S1: Modal proportions (vol%) of (clockwise, from top left) modern MORB, B30, pyrolite in the Archean, Archean harzburgitic lithosphere, modern harzburgitic lithosphere, and pyrolite in the modern day. Phase equilibria were calculated using *Perple_X* (Connolly, 2009) with thermodynamic data (after Stixrude and Lithgow-Bertelloni, 2011) except for B30 (Archean crust). For B30, experimental data in the present study were used at 20–35 GPa and extrapolated based on *Perple_X* model for 10–20 GPa. We used the temperature model of the subducting slab from Klein et al. (2017). Modern (Brown and Shankland, 1981) and Archean geotherms (elevated by 200 K with respect to modern geotherm) were used for pyrolite, respectively.

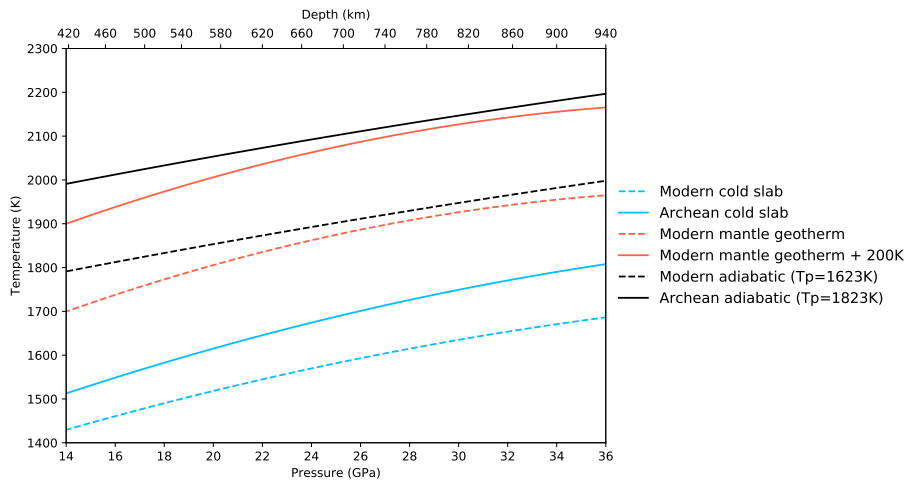


Figure S2: Temperature gradients of subducting slabs (blue) and pyrolite (red), and mantle adiabatic gradients (black). Solid and dashed lines represent the modern day and Archean. Temperature gradients of subducting slabs are from Klein et al. (2017). 0.4 K/km is used to plot the mantle adiabats.

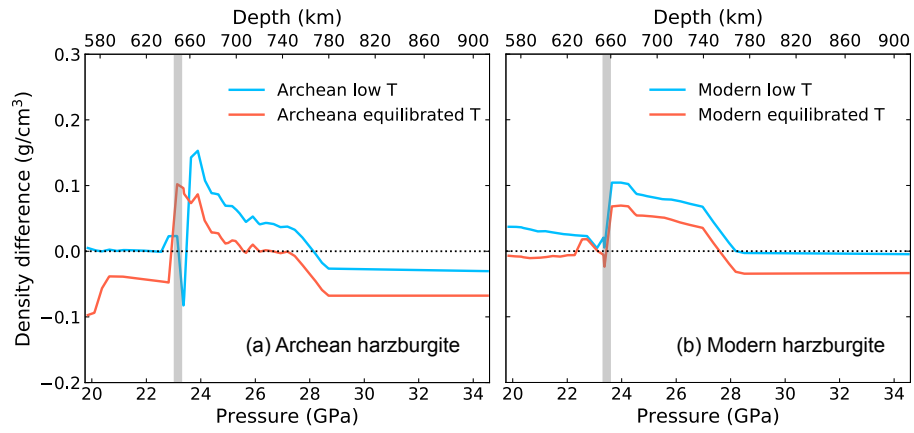


Figure S3: The density differences between harzburgite and the pyrolitic surrounding mantle in (a) the Archean and (b) the modern day. The densities were calculated using *Perple_X* (Connolly, 2009) with the thermodynamic data set (Stixrude and Lithgow-Bertelloni, 2011). The depths of the post-spinel transition in pyrolite is marked by the vertical grey bars. Information on the temperature profiles can be found in Table S3.

Table S1: Run table for in situ experiments of B30.

Sample#	Run#	Medium	Dur. (min)	Au V (Å ³)	P ^a (GPa)	P_err (GPa)	T (K)	T_err (K)	Phase assemblage
218	7	Ne	4.5	61.66	33.62	0.75	2356	100	Brg+CaPv
	13	Ne	5	61.91	32.54	0.75	2382	100	Brg+CaPv
	15	Ne	5	61.65	31.06	0.75	2012	100	Brg+CaPv
812	107	Ar	3.5	62.26	29.13	0.75	2160	100	Brg+CaPv
	76	Ar	2.5	62.51	24.67	0.76	1719	100	Brg+CaPv
	122	Ar	5	61.88	28.06	0.75	1766	100	Brg+CaPv
	102	Ar	3	62.18	28.87	1.09	2072	145	Brg+CaPv
914	96	Ar		62.74	25.98	0.76	2040	100	Brg+CaPv
	114	Ar	4	62.64	25.68	0.76	1938	100	Brg+CaPv
	16	Ar	2.5	65.07	13.09	0.78	1592	100	Gt+Rw
1415	54	Ar	3	63.61	21.20	0.76	1906	100	Gt+Rw
	137	Ar	3	63.15	21.31	0.76	1663	100	Gt+Rw
	38	Ar	3.5	62.70	22.64	0.76	1573	100	Gt+Rw+CaPv+(Brg) ^c
1514	93	Ar	3	63.11	23.79	1.64	1966	215	Gt+Brg+CaPv
	44	Ar	3.5	62.68	25.72	0.76	1966	100	Gt+Brg+CaPv
1615	82	Ar	2	63.07	24.25	0.76	2004	100	Gt+Brg
	86	Ar	5	62.89	23.44	0.76	1791	100	Gt+Brg
	97	Ar	4	62.61	24.89	0.76	1816	100	Gt+Brg+(CaPv) ^c
	41	Ar	6	63.05	24.06	0.76	1966	100	Gt+Brg+CaPv
	46	Ar	4	63.15	24.92	0.76	2140	100	Gt+Brg+CaPv
	63	Ar	5.5	62.82	23.66	0.76	1777	100	Gt+Brg+CaPv
	76	Ar	6.5	62.78	24.69	0.76	1889	100	Gt+Brg+CaPv
	51	Ar	3	62.99	23.18	0.76	1820	100	Gt+Brg+CaPv
1912	28	NaCl	2 sec.	60.70	34.16	0.74	1737	100	Brg+CaPv
	91	NaCl	2 sec.	61.21	33.28	0.75	2003	100	Brg+CaPv
2115	127	Ar	2	61.99	29.40	0.75	2014	100	Brg+CaPv
2715	167	Ar	1.5	62.94	26.65	0.76	2247	100	Gt+Brg+CaPv
	189	Ar	3	62.72	25.08	0.76	1904	100	Gt+Brg+CaPv
	196	Ar	5	62.54	25.88	0.76	1899	100	Gt+Brg+CaPv
	20	Ar	5	63.82	18.90	0.77	1718	100	Gt+Rw
	81	Ar	4	63.21	22.56	0.76	1834	100	Gt+Rw
	86	Ar	1	63.56	20.75	0.76	1822	100	Gt+Rw
	89	Ar	2	63.92	20.24	0.83	1947	108	Gt+Rw
	95	Ar	1.5	63.36	18.98	0.76	1476	100	Gt+Rw
	99	Ar	2	62.91	21.09	0.76	1496	100	Gt+Rw
	114	Ar	3.5	63.38	20.92	0.76	1746	100	Gt+Rw
	141	Ar	2	63.50	20.04	0.76	1695	100	Gt+Rw
4530	98	KCl	4	63.38	23.77	1.25	2120	164	Gt+Brg
	91	KCl	5.5	62.81	25.83	1.31	2058	173	Gt+Brg+CaPv
	119	KCl	5	62.59	24.24	1.06	1715	140	Gt+Brg+CaPv
	25	KCl	5	62.83	23.18	0.83	1724	110	Gt+Brg+CaPv
	38	KCl	7.5	63.14	24.89	1.22	2126	161	Gt+Brg+CaPv
4430 ^b	-	Ar	NA	62.02	19.52	NA	1900	150	Gt+Rw

^a Pressure was determined by Au scale (Dorogokupets and Dewaele, 2007) and corrected according to (Ye et al., 2017).

^b Pressure was measured at 300 K.

^c The phases in parenthesis were identified with the weak X-ray diffraction peaks.

Table S2: Garnet compositions of pyrolite, B30, and modern MORB.

	20.5 GPa 2,073 K	23 GPa 1,900 K	24 GPa 2,023 K
Wt%	Pyrolite ^a	B30 ^b	MORB ^c
SiO ₂	50.8	49.7	40.7
TiO ₂	0	0	0.7
Al ₂ O ₃	10.6	8.6	20.6
FeO	5.0	11.8	14.4
MnO	0	0	0.2
MgO	28.0	20.9	12.3
CaO	4.6	9.0	8.1
Na ₂ O	0.3	NA	2
K ₂ O	0.2	0	0
Cr ₂ O ₃	0.7	0	0.1
Total	100.1	99.3	99.1

^a Hirose (2002)

^b This study

^c Hirose and Fei (2002)

Table S3: Methods used for the density calculation in this study. Exp: from our experiments; PX: from Perple_X calculation.

Mineralogy	Archean	Modern
Crust	EXP	PX
Harzburgite	PX	PX
Pyrolite	PX	PX
Temperature profile	Archean	Modern
Low	K17 ^a	K17 ^a
Equilibrated	B81+200 K ^c	B81 ^b

^a Klein et al. (2017)

^b Brown and Shankland (1981)

^c 200 K added to the modern mantle geotherm.